University of Glasgow | School of Engineering

Assembly of Electronics and Optoelectronics with Optoelectronic Tweezers

Yongpeng LIU

Supervisor: Dr. Steven L. Neale

August 2016

A thesis submitted in partial fulfilment of the requirements for the degree of
Master of Science in Nanoscience and Nanotechnology

Abstract

Optoelectronic Tweezers (OET) is a relatively new micro- and nanoscale manipulation technique that takes advantage of both optical tweezers and dielectrophoresis (DEP). Based on light induced dielectrophoresis (LIDEP), the virtual electrodes which are created by light allow continuous control and massively parallel manipulation over a large operational area with a low required optical power and a high accuracy.

The developments and the physical regimes of OET are reviewed in the first two chapters.

List of Objectives

General objectives:

The aim of this project is to investigate the capacity of optoelectronic tweezers in creating electrical connection and assembling micron level electronic and optoelectronic components.

Specific objectives:

- To characterise the accuracy in manipulating of optoelectronic tweezers;
- To investigate moving speed and exerted dielectrophoresis force of micro-objects;
- To analyse freeze-drying and melt process;
- To build a good electrical connection with optoelectronic tweezers;
- To assemble discrete micro level electronic and optoelectronic components with optoelectronic tweezers.

Acknowledgements

I would like express my thanks towards my supervisor, Dr. Steven Neale for his useful comments, guidance and unwavering patience through the whole learning process of this master project. Furthermore I would like to thank Dr. Shuailong Zhang for introducing me to the topic as well for the support on the way. Thanks to Professor Jonathan Cooper for bring me in the biomedical engineering research group at the University of Glasgow.

Thanks to Dr. Erdan Gu (University of Strathclyde) for providing the GaN micro-LEDs, Justin Sperling for providing the carbon nanotubes, Dr. Joan Juvert (Ghent University-IMEC) for helping with simulation and the James Watt Nanofabrication Centre (Glasgow, UK) for helping with devices fabrication.

Publications

Shuailong Zhang, **Yongpeng Liu**, Joan Juvert, Pengfei Tian, Jean-Claude Navarro, Jonathan M. Cooper, and Steven L. Neale. (2016). Use of optoelectronic tweezers in manufacturing-accurate solder bead positioning. ***Applied Physics Letters***, Volume 109, Number 22, pp. 221110.
http://dx.doi.org/10.1063/1.4971348

Shuailong Zhang, **Yongpeng Liu**, Yang Qian, Weizhen Li, Joan Juvert Sandez, Pengfei Tian, Jean-Claude Navarro, Alasdair Clark, Erdan Gu, Martin D. Dawson, Jonathan M. Cooper, and Steven L. Neale. (2017). Manufacturing with light-micro-assembly of opto-electronic microstructures. ***Optics Express***, Vol. 25, Issue 23, pp. 28838-28850.
https://doi.org/10.1364/OE.25.028838

Nomenclature

a-Si:H = Hydrogenated amorphous silicon

AC = Alternating Current

CCD = Charge-Coupled Device

CMOS = Complementary metaloxidesemiconductor

DC = Direct Current

DEP = Dielectrophoresis

EDL = Electrical Double Layer

ET = Electrothermal

ITO = Indium tin oxide

LACE = Light-actuated AC Electroosmosis

LED = Light-Emitting Diode

LIDEP = Light Induced Dielectrophoresis

LOET = Lateral-field Optoelectronic Tweezers

OET = Optoelectronic Tweezers

PCB = Printed Circuit Board

PECVD = Plasma-enhanced Chemical Vapor Deposition

PMMA = Poly(methyl methacrylate)

RIE = Reactive-ion Etching

SEM = Scanning Electron Microscopy

SMT = Surface-Mount Technology

V_{pp} = peak-to-peak Voltage

Contents

List of Tables

List of Figures

Chapter 1

Introduction

The manipulation of micro- and nanoscale objects including biological cells, DNA, nanowires and microspheres plays an important role in biology and physical chemistry. Conventional micro-manipulation techniques such as optical tweezers (**Fig.1.1**(**a**)) and dielectrophoresis (DEP) have their advantages and limitations. Arthur Ashkin, Steven Chu, and their co-workers first introduced optical tweezers at AT&T Bell Laboratories[1],[2]. It uses optical gradient force to manipulate specific single object[3],[4]. Optical tweezers can precisely trap as small as 5 nm[5],[6] and achieve 100 pN force[7],[8],[9]. Furthermore, diffractive beam splitter with computer-generated holograms can convert single input laser beam into several beams in order to form multiple optical traps (**Fig.1.1**(**b**)), also known as holographic optical tweezers[10],[11]. However, a strongly focused laser beam (optical intensity greater than 10^5 W/cm^2) is required in trapping and moving objects[12], which may cause damage to biological cells due to local heating or two-photon absorption[13]. The application of optical tweezers is also limited in massively parallel manipulation of objects[14]. As for DEP, it has extensive application to cell separation[15],[16] and particle filtration[17], which can reach a high throughput[18]. However, single particle manipulation can hardly be achieved via conventional DEP. Conventional DEP can accomplish parallel manipulation with the help of complementary metaloxidesemiconductor (COMS) technology (**Fig.1.1**(**c**))[19] but fixed metal electrodes are required to form trapping patterns.

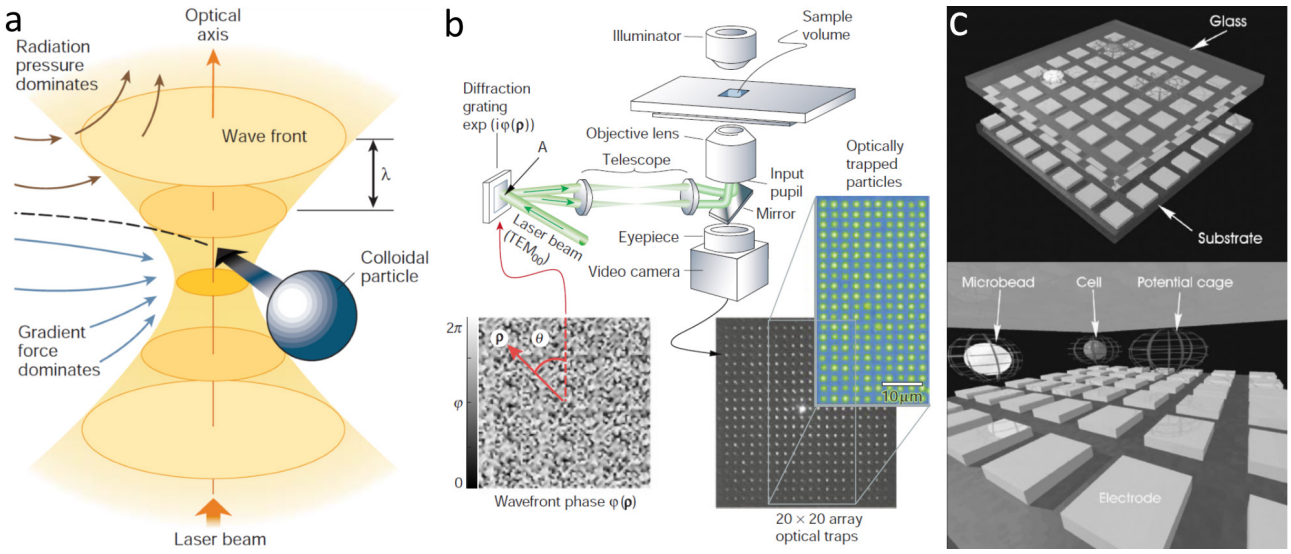

Figure 1.1: (**a**) Working principle of optical tweezers. (**b**) An optical tweezers system with 20 × 20 array optical traps created by computer-generated holograms. The input laser is a collimated TEM_{00} beam. (**c**) A 0.35 μm node CMOS technology with an array of 320 × 320 actuation electrodes is being used to manipulate and detect individual cell. Figure reproduced with permission from: **a-b**,ref.[14], ©2003 Nature Publishing Group; **c**,ref.[19], ©2003 IEEE.

Optoelectronic Tweezers (OET) is a novel micro- and nanoscale manipulation technique which takes advantage of both optical tweezers and DEP. Optical tweezers directly converts optical energy to mechanical energy while DEP directly converts electrical energy to mechanical energy. However, OET has an indirect energy conversion mechanism from optical energy to mechanical energy. Light first creates virtual electrodes on the bottom photoconductive surface. Based on electrokinetic mechanism similar to DEP, these light induced virtual electrodes then convert electrical energy to mechanical energy. The invention of reconfigurable virtual electrodes allows continuous control and massively parallel manipulation over a much larger operational area than optical tweezers which needs a focused optical field. Moreover, a much lower optical power than optical tweezers is required to create these virtual electrodes and produce DEP.

Based on light induced dielectrophoresis (LIDEP), OET was first demonstrated by Pei Yu Chiou et al. in 2003[20]. The liquid solution containing 25 μm diameter latex particles is sandwiched between a top indium tin oxide (ITO) coated glass layer and a bottom photoconductive layer with an AC voltage be applied between the top ITO and the bottom aluminum electrodes (**Fig.1.2**(**a**)). They achieved 187 pN trapping force, thereby successfully transporting the latex particles at the speed of 397 μm/s with the optical power of 100 μW.

In 2005, Pei Yu Chiou et al. improved the structure of OET (**Fig.1.2**(**b**)) that allows a high resolution patterning of electric fields[21]. Compared with the original structure (**Fig.1.2**(**a**)), the bottom photosensitive surface consists of two photoconductive layer, 1 μm undoped hydrogenated amorphous silicon (a-Si:H) layer and 50 nm heavily doped a-Si:H layer. The original aluminum layer on the bottom surface is replaced by an ITO-coated glass layer. The improved OET device therefore achieved massively (15,000) parallel manipulation of 4.5 μm diameter polystyrene beads across a 1.3 mm $\times$ 1.0 mm area (**Fig.1.2**(**c**)). In addition, the dielectric differences between biological cells (size, internal conductivity and membrane properties)[22],[23],[24] permit OET to selectively collect live cells from a mixture of live and dead cells (**Fig.1.2**(**d**)). The minimum required optical power to sustain trap is 100,000 times less than optical tweezers.

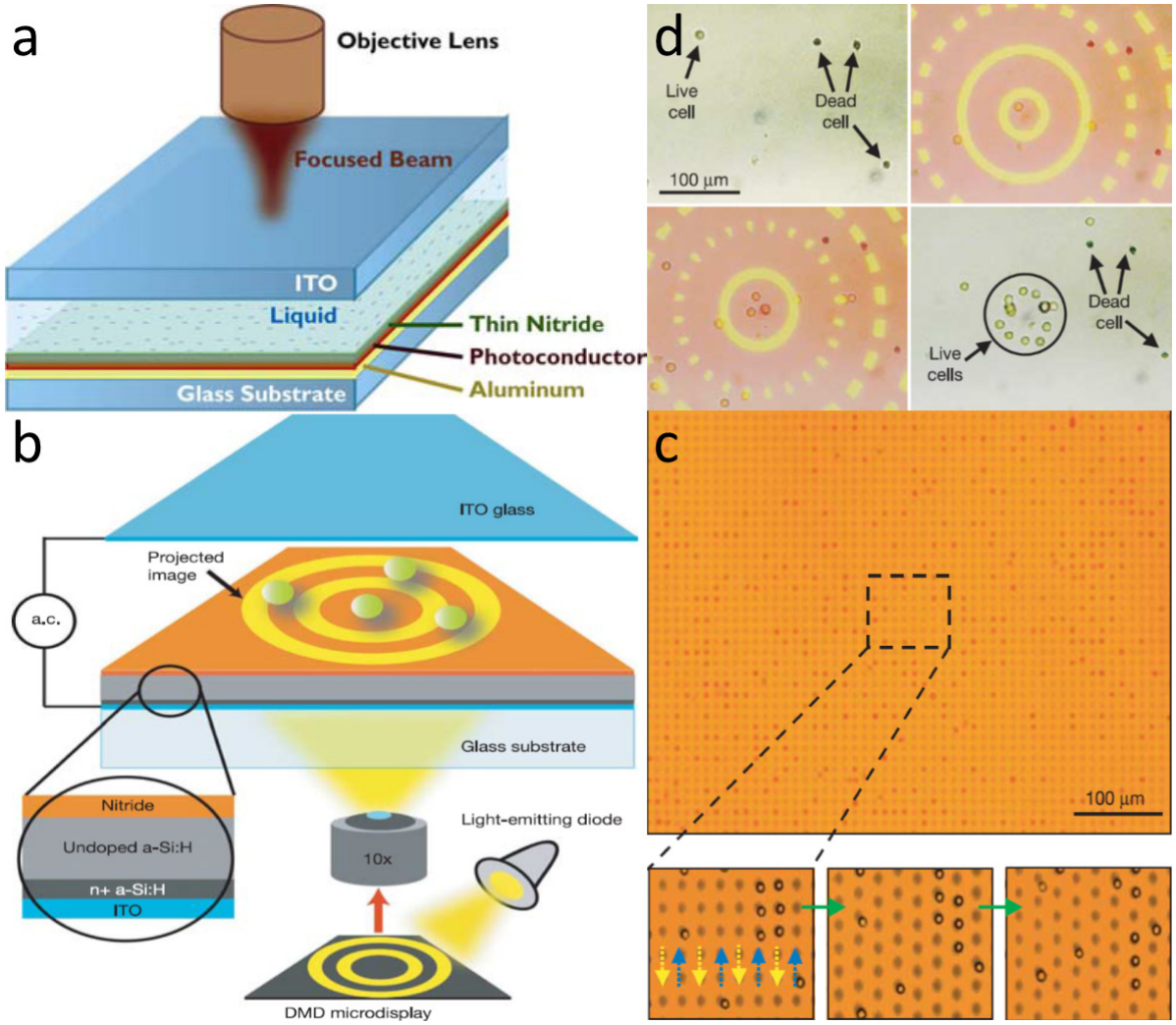

Figure 1.2: (**a**) Schematic diagram of the first presented OET device. (**b**) An improved OET device structure. (**c**) Massively parallel trapping and transportation of 4.5 μm diameter polystyrene beads. (**d**) Cell separation between live and dead cells. Figure reproduced with permission from: **a**,ref.[20], ©2003 IEEE; **b-d**,ref.[21], ©2005 Nature Publishing Group.

Steven L. Neale et al. investigated the resolution, the achieved trap stiffness and the required optical power (where the trap is strongest) between the optical trap and the LIDEP trap in 2007[25]. They suggested that the minimum LIDEP trap size depends not only on the optical pattern (diffraction limit) and the photoconductive materials (diffusion length)[26] but also the illuminated conductivity. They found that the penalty of reduced trapping strength is the only way to create a smaller LIDEP trap. Based on the finite element simulation (COMSOL Multiphysics), they found that the illuminated conductivity on photoconductive surface will vary in a Gaussian profile (**Fig.1.3**(**a**)) and the LIDEP trap will larger than the set optical spot when a high conductivity is reached. **Fig.1.3**(**b**) shows that the DEP force (directly proportional to the gradient of the electric field squared) scales as the illuminated conductivity. Furthermore, they operated OET when the strongest LIDEP trap is achieved and used stiffness to quantify the strength of the LIDEP trap. Result shows that the LIDEP trap is 470±94 times stiffer per power ratio than a standard optical tweezers trap.

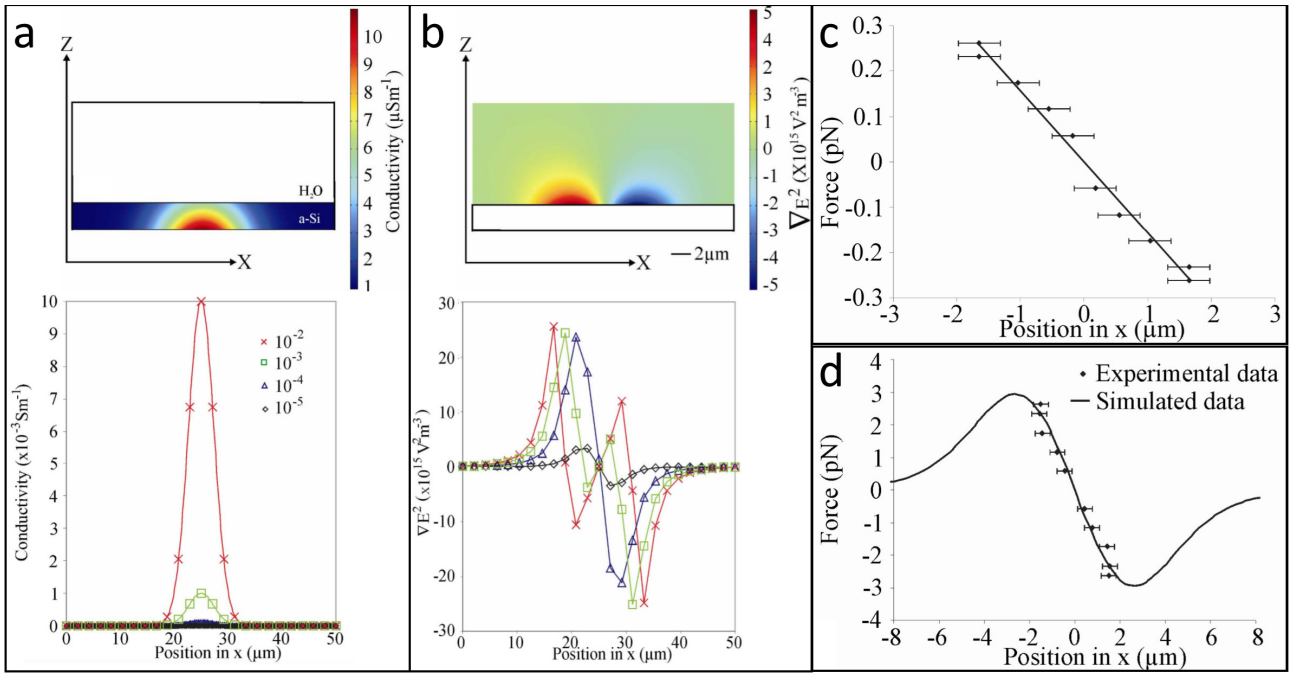

Figure 1.3: The simulation of (**a**) the illuminated conductivity and (**b**) the gradient of the electric field squared. The profiles of (**c**) the LIDEP trap and (**d**) a standard optical trap under the same experimental measurement. Figure reproduced with permission from: **a-d**,ref.[25], ©2007 Optical Society of America.

Aaron T. Ohta et al. first presented a modified single-sided OET device named Lateral-field Optoelectronic Tweezers (LOET) in 2007[27]. Compared with conventional OET, LOET has

electrode arrays on the bottom surface (**Fig.1.4**(**a**)). The voltage is applied laterally on these electrode arrays, therefore, LOET can produce an electric field which parallel to the substrate. After the deposition of a-Si:H layer, these electrode arrays are etched by Reactive-ion Etching (RIE), stopping on the ITO layer. Polymer micro-particles with 25 μm and 45 μm diameter have been manipulated successfully by LOET. A year later, Aaron T. Ohta et al. reported a parallel manipulation and assembly of individual silver nanowire based on LOET (**Fig.1.4**(**b**)-(**d**))[28].

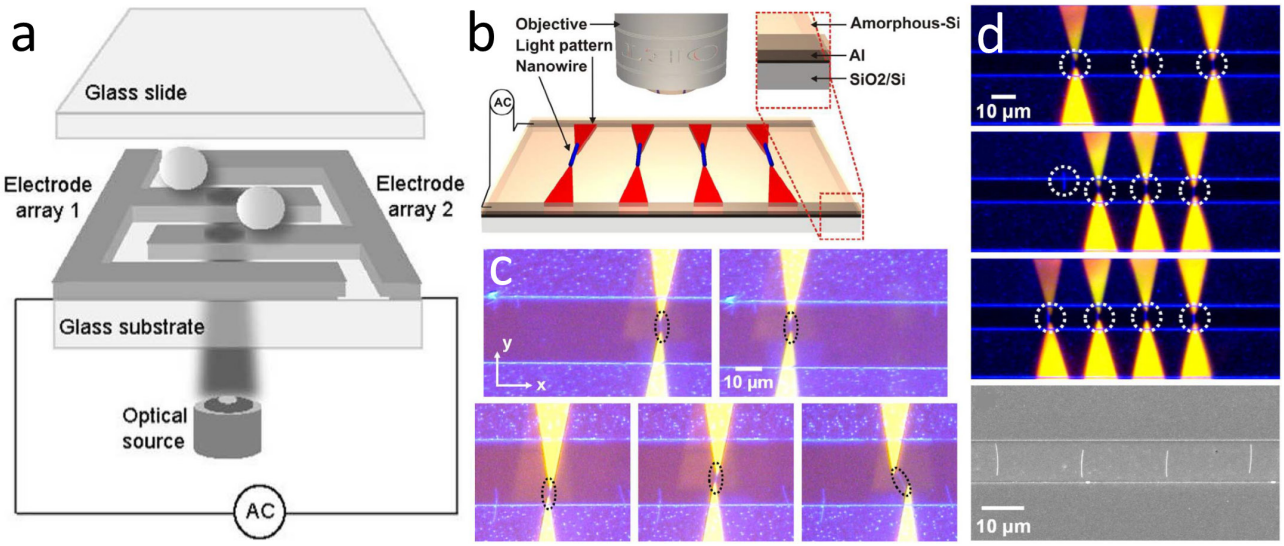

Figure 1.4: (**a**) Schematic diagram of the LOET device. (**b**) Schematic diagram of the LOET device for nanowire assembly. (**c**) Individually trapping of silver nanowires. (**d**) Assembly of silver nanowires. Figure reproduced with permission from: **a**,ref.[27], ©2007 IEEE; **b-d**,ref.[28], ©2008 IEEE.

Some non-specific interactions such as Van der Waals force, hydrophobic effect and electrostatic interactions may interfere with the effectiveness of the conventional OET. A specific problem that results from these non-specific interactions is particle being adsorbed to the surface of ground layer (**Fig.1.5**(**a**)-(**b**)). In order to solve this problem and achieve a higher particle trapping efficiency, Hyundoo Hwang et al. demonstrated a novel three-dimensional OET in 2008[29]. A three-dimensional OET has photoconductive layer on both top and bottom surface, which allows particle to be trapped at the middle of the liquid chamber (**Fig.1.5**(**c**)). Under the same experimental conditions of 20 V_{pp} at 100 kHz frequency and 120 μm liquid chamber height, they explored the rate of absorbed particles and the maximum moving speed of particles over a range of bead (polystyrene) diameter. **Fig.1.5**(**d**) shows that more than half of the particles

are absorbed to the surface of ground layer in the conventional OET while only a few particles are absorbed in the three-dimensional OET. Result also shows that the three-dimensional OET can move particles to a higher speed than the conventional OET (**Fig.1.5**(**e**)).

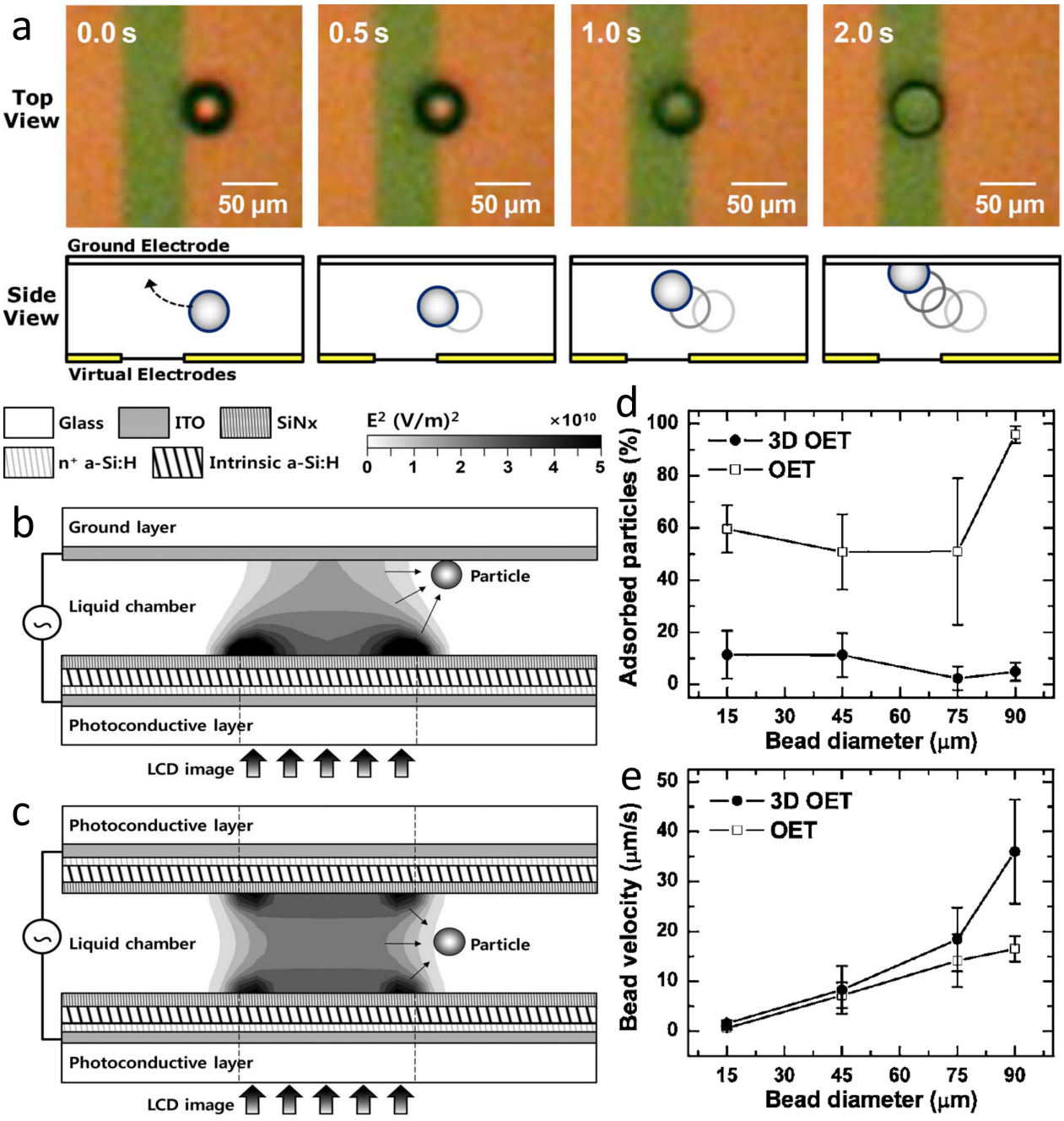

Figure 1.5: (**a**) The process of particle absorption in a conventional OET. (**b**) Schematic diagram of a conventional OET. The non-specific interactions result in particle absorption. (**c**) Schematic diagram of the three-dimensional OET with particle being trapped at the middle of the liquid chamber. (**d**) The rate of absorbed particles and (**e**) the maximum moving speed of particles over over a range of bead diameter in a conventional OET and a three-dimensional OET. Figure reproduced with permission from: **a-e**,ref.[29], ©2008 American Institute of Physics.

To achieve a more precise nanoscale manipulation, Arash Jamshidi and Peter J. Pauzauskie et al. demonstrated a dynamic manipulation of individual semiconducting nanowire and metallic nanowire with diameter below 20 nm via OET (**Fig.1.6**(**a**)) in 2008[30]. The first challenge on manipulation nanoscale objects is that the DEP force decreases rapidly with the object size (**Fig.1.6**(**g**)). They therefore considered to use one-dimensional nanostructure, nanowire. Without applied voltage, the LIDEP trap is invalid therefore the silicon nanowire will experience Brownian motion (**Fig.1.6**(**c**)). An applied voltage can activate the OET device so that the long axis of the silicon nanowire will first align with the electric field (**Fig.1.6**(**d**)) then being trapped by the LIDEP trap (**Fig.1.6**(**e**)). By using particle tracking image analysis[31], Arash Jamshidi characterised the Brownian motion and manipulating trajectory of nanowires[32]. **Fig.1.6**(**e**) shows the whole trajectory of the nanowire during manipulation. Furthermore, a dynamic separation method was found by comparing the maximum experimental trapping speed between individual silicon nanowire and silver nanowire (**Fig.1.6**(**e**)). An 8 V_{pp} leads to a 125 μm/s speed for silver nanowire but a 2 μm/s speed for silicon nanowire. Thus, an 8 V_{pp} can be set as the separation voltage to separate silicon nanowire and silver nanowire. They achieved large area manipulation based on the digital micro-mirror spatial light modulator[33].

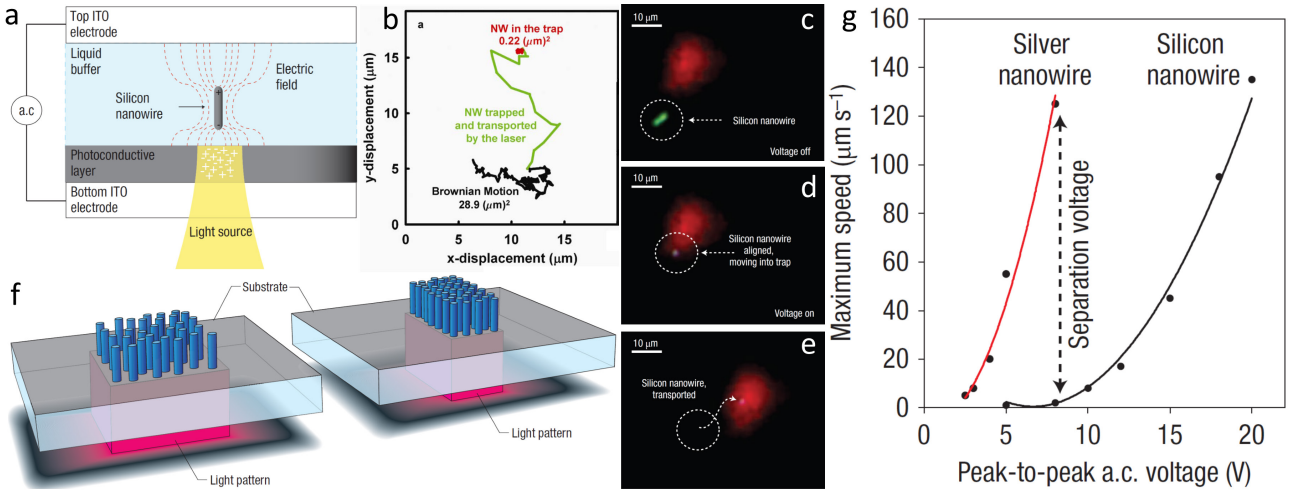

Figure 1.6: (**a**) Schematic diagram of the OET device. (**b**) The trajectory of an individual silicon nanowire. (**c**) An individual silicon nanowire is experiencing Brownian motion before the voltage is applied. (**d**) The long axis of the silicon nanowire aligns with the electric field. (**e**) The silicon nanowire is trapped by the LIDEP trap. (**f**) Large-scale assembly of nanowires. (**g**) The maximum experimental trapping speed of individual silicon nanowire and silver nanowire over a range of V_{pp}. Figure reproduced with permission from: **a,c-g**,ref.[30],[33] ©2008 Nature Publishing Group; **b**,ref.[32], ©2009 Arash Jamshidi.

In 2009, Arash Jamshidi et al. utilized various electrokinetic forces (dielectrophoresis, light-actuated AC electroosmosis[34],[35] and electrothermal flow[36]) to demonstrate a novel OET optofluidic platform, NanoPen (**Fig.1.7**(**a**)-(**b**))[37]. NanoPen allows a real-time reconfigurable manipulation and permanent immobilization of nanoparticles over a large (thousands of square micrometers) area (**Fig.1.7**(**c**)-(**d**)). They used NanoPen to pattern 90 nm diameter gold nanoparticles therefore achieved an enhancement factor of 1.3×10^7 in surface-enhanced Raman spectroscopy. NanoPen has a great potential in nanofabrication and biological sensing.

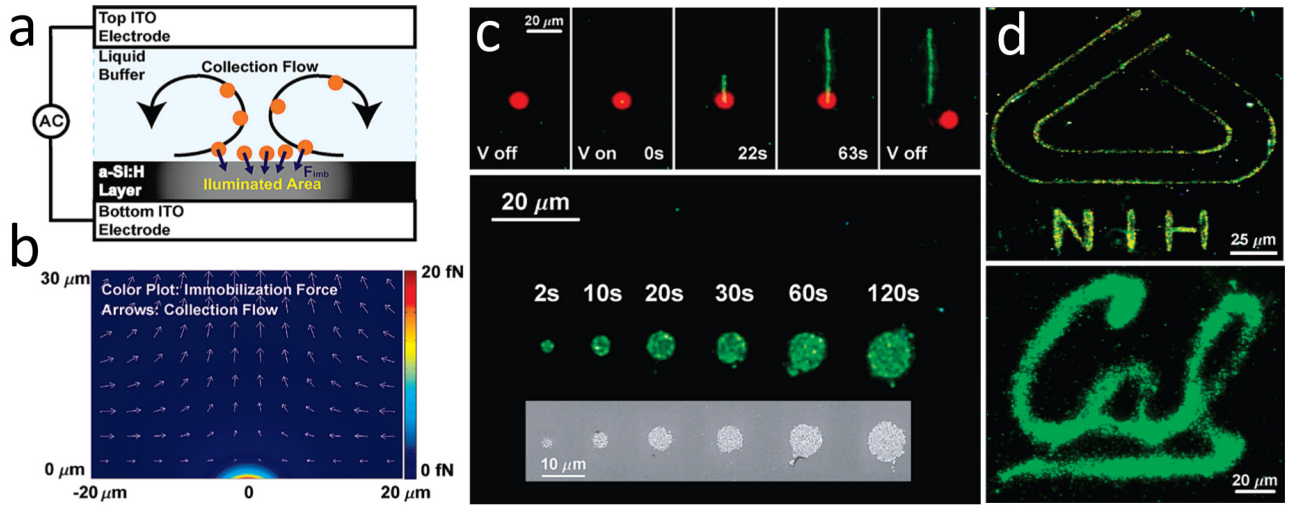

Figure 1.7: (**a**) Schematic diagram of the NanoPen. (**b**) Finite element simulation of the NanoPen operation present the light-actuated AC electroosmosis and electrothermal flow. (**c**) Real time patterning process of the NanoPen with red patterning beam spot and green patterned 90 nm diameter gold nanoparticles. (**d**) Patterned logo of 'NIH' and 'CAL' using NanoPen. Figure reproduced with permission from: **a-d**,ref.[37], ©2009 American Chemical Society.

They also demonstrated the OET trapping of gold nanoparticles (60 to 250 nm diameters) with 68 μm/s translational velocities[38]. They estimated that the light induced heating in OET will be lower than 0.1 °C. While the light induced heating in optical tweezers will be higher than 55 °C due to the high required optical power[39]. OET gets rid of the excessive heating problem, which proves that the OET is suitable for biological applications.

Making use of the light induced heating in OET, Aaron T. Ohta et al. successfully demonstrated the thermocapillary movement of gas bubbles in a silicone oil medium[40]. The maximum moving speed of bubbles is 1.5 mm/s with bubbles volumes ranging from 19 pl to 23 nl. Since gas bubbles can play a part in microfluidics, including blender[41], valve[42], pump[43] and switch[44], OET therefore has potential applications in microfluidics.

Steven L. Neale et al. used a data projector as the light source rather than LED or laser to create the virtual electrodes on photoconductive surface in 2009[45]. They suggested that a greater trap stiffness can be found at the edges of the optical spot therefore a similar size between optical spot and object may achieve a constant stiffness of the trap. They succeeded in creating a trap with constant stiffness of 3×10^{-6} N/m so that the HeLa cell can be trapped up to 50 μm/s.

Three years later, Steven L. Neale et al. proposed a quantitative measurement of medical condition via OET[46]. By applying a 20 V_{pp} at 1.5 MHz frequency with 10 mSm^{-1} medium conductivity, the Feret diameter of murine erythrocytes can be changed around 10% by OET. Thus, an important indicator of cell health, the relative stiffness of erythrocytes, can be measured. This method has the potential applications in obesity related diabetes and treatment effect.

Besides biological applications, the capacity of OET in manipulating metallic and semiconducting objects holds great potential for constructing circuits since the development of design and manufacturing keeps scaling the size of electronic components. Mainstream technology for mass production of electronic devices is surface-mount technology (SMT) in which discrete electronic components are mounted directly onto the surface of printed circuit board (PCB) by mechanical manipulator arm. The priority in circuit construction is to provide electrical connections among components, which is the first step of applying OET in circuits construction.

Shuailong Zhang et al. succeeded in assembling silver nanowires to form a 150 μm conductive path between two isolated metal electrodes (**Fig.1.8**(**a**)-(**b**)) in 2016[47]. Current-voltage characteristic shows that the resistance between the two isolated metal electrodes drops to around 700 Ω after assembling sliver nanowires (**Fig.1.8**(**c**)). They also investigated the capacity of OET for moving a micro-resistor with the current smallest standard size of 400 $\times$ 200 μm (**Fig.1.8**(**d**)-(**e**))[48], which proves the potential applications in assembling electronic components via OET. In the same year, Joan Juvert et al. reported the accuracy of positioning standard Fabry-Pérot InP semiconductor laser die with 250 μm across and 100 μm thick[49], which proves the potential applications in assembling optoelectronic components via OET.

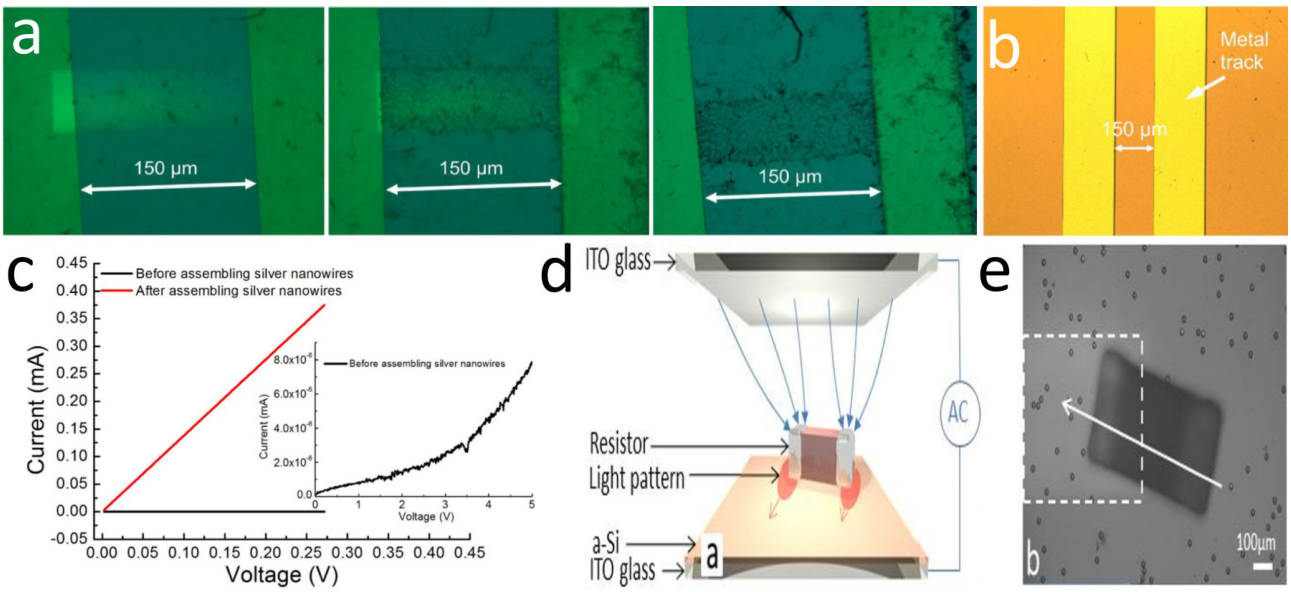

Figure 1.8: Optical microscope images of (**a**) assembling silver nanowires to form a 150 μm long conductive path between two isolated metal electrodes and (**b**) before assembling. (**c**) Current-voltage characteristic of two isolated metal electrodes before and after the form of conductive path. The resistance was effectively brought down to around 700 Ω after assembling silver nanowires. (**d**) Schematic diagram of moving a micro-resistor via OET. (**e**) Optical microscope image of the mircoresistor moved by OET. Figure reproduced with permission from: **a-c**,ref.[47], ©2016 SPIE; **d-e**,ref.[48], ©2016 Shuailong Zhang.

Previously published works indicate that OET can be used to create electrical connection, but 700 Ω is too high to act as an ideal conducting path. Therefore, we are trying to assemble different types of conducting materials including solder and carbon nanotubes (CNTs) in order to create a better electrical connection with a lower resistance. More specifically, we are going to investigate how accurate can the assembly process be done by OET and the capacity of OET for manipulating micro-LED. Since the manipulation process is surrounded by liquid solution, a way of removing liquid before current-voltage characteristic needs to be found.

Chapter 2

Theory

2.1 Physical Regimes in Optoelectronic Tweezers (OET)

2.1.1 Light Induced Dielectrophoresis (LIDEP)

Dielectrophoresis (DEP) is the electrical analogue of optical tweezers in which a non-uniform electric field can exert force on a dielectric particle[50],[51],[52]. Conventional DEP is produced by fixed metal electrodes which need additional fabrication process and limit the flexibility of the device. Optoelectronic Tweezers (OET) solve the problem by using light induced dielectrophoresis (LIDEP) to create virtual electrodes. Particles can be attracted or repelled at the area where the highest electric field intensity gradient achieved. The non-uniform electric field can induce dipoles on particles so that each end of a particle will have unequal charge. The forces at each end of a particle therefore are unequal, which results in a net force. The net force can be used to describe the DEP force as[53]:

$$F_{DEP} = p\nabla E \tag{2.1}$$

where p is the dipole moment of the particle and E is the first term of the Taylor series expansion of the electric field. The time-averaged DEP force of a spherical particle is defined as[53]:

$$F_{DEP} = 2\pi r^3 \varepsilon_m Re[K(\omega)] \nabla E_{rms}^2 \tag{2.2}$$

where r is the radius of the particle, ε_m is the permittivity of the surrounding medium, E_{rms}^2 is the root mean square electric field strength and $Re[K(\omega)]$ is the real part of the Clausius-Mossotti (C.M.) factor which is defined as:

$$K(\omega) = \frac{\varepsilon_p^* - \varepsilon_m^*}{\varepsilon_p^* + 2\varepsilon_m^*}, \varepsilon_m^* = \varepsilon_m - j\frac{\sigma_m}{\omega}, \varepsilon_p^* = \varepsilon_p - j\frac{\sigma_p}{\omega} \tag{2.3}$$

where ε_p is the permittivity of the particle, ω is the angular frequency of the electric field, σ_m and σ_p are the conductivities of the surrounding medium and the particle, respectively[50]. The frequency therefore can be used to adjust the magnitude of C.M. factor, leading to a frequency-dependent DEP force[54]. For particles that experience a positive DEP force will be attracted to the highest electric field intensity gradient, and vice versa, a negative DEP force will repel particles from the highest electric field intensity gradient[53].

Concerning biological cells manipulation, the DEP force (**Eq.(2.3)**) has to be modified due to the non-homogeneous characteristic of biological cells. By assuming the radius of the cell interior is much larger than the thickness of the cell membrane[16], an effective permittivity that considered both the cell membrane and the cell interior is given by:

$$\varepsilon_p^* = C_{mem}^* \frac{3r\varepsilon_{int}^*}{3\varepsilon_{int}^* + 3C_{mem}^* r} \tag{2.4}$$

where ε_{int}^* is the complex internal conductivity of the cell, r is the radius of the cell interior and C_{mem}^* is the membrane capacitance which is defined as:

$$C_{mem}^* = \frac{\varepsilon_{mem}}{d} - \frac{j\sigma_{mem}}{d} \tag{2.5}$$

where d is the thickness of the cell membrane. ε_{mem} and σ_{mem} are the permittivity and conductivity of the cell membrane, respectively. The unique characteristics of different type of biological cells enable the capacity of cell separation via DEP force.

If a particle is being dragged in a liquid medium, the particle will experience a net hydrodynamic force called drag force. The drag force that exerts on a spherical particle can be described as[55]:

$$F_{drag} = 6\pi r\eta\nu \tag{2.6}$$

where r is the Stokes radius (in our experiment it equals to the radius of the spherical particle), η is the viscosity of the liquid medium and ν is the velocity of the moving particle. The Faxen's correction should be considered since the particle is close to the surface[56]. The drag force therefore should be described as[25]:

$$F_{drag} = \frac{6\pi r\eta\nu}{(1 - \frac{9}{16}(\frac{r}{h}) + \frac{1}{8}(\frac{r}{h})^3 - \frac{45}{256}(\frac{r}{h})^4 - \frac{1}{16}(\frac{r}{h})^5)} \tag{2.7}$$

where h is the distance between the surface and the centre of the spherical particle[56]. By measuring the speed of the particle, the DEP force can be calculated due to:

$$F_{DEP} = F_{drag} \tag{2.8}$$

2.1.2 Light-actuated AC Electroosmosis (LACE)

An applied electrical potential across micro-channels will lead to the motion of fluid. This fluid flow called electroosmosis that is often employed in the use of microfluidic pumps in microfluidics systems[57],[58]. An electrical double layer (EDL) on an ionic fluid is formed by the application of the electrical potential. Charged ions in the EDL will be driven by the tangential component of electric field at a slip velocity which is given by the Helmholtz-Smoluchowski equation[59]:

$$\nu_{SLIP} = -\frac{\varepsilon\zeta E_t}{\eta} \tag{2.9}$$

where ε is the permittivity of the surrounding medium, ζ is the zeta potential, E_t is the tangential component of electric field and η is the fluid viscosity[54].

Either a DC bias[57],[60] or an AC bias[61],[62] can be used to generate electroosmosis. In the DC mode, the zeta potential ζ is determined by the materials properties of micro-channels and the ionic strength of electrolytes[35]. In the AC mode, the ionic charge at the surface of the EDL will switch polarity to the applied electrical potential so that a steady AC electroosmosis flow in one direction is formed[32],[63]. The virtual electrodes in OET device lead to a tangential electric field therefore a slip velocity is produced, resulting in a light-actuated AC electroosmosis (LACE). **Fig.2.1**(**a**) demonstrates the working principle of LACE in OET. The interaction among the virtual electrodes on photoconductive layer, tangential component of electric field and ionic charges in the EDL results in a microfluidic vortex. The LACE can be modelled as an equivalent circuit (**Fig.2.1**(**b**)) in which the EDL acts as a capacitor in series with resistors accounting for the photoconductive layer and the liquid medium[35]. The thickness d of the EDL follows the GouyChapman theory[18]:

$$d = (\frac{2\sigma_m z^2 e}{\mu_m \varepsilon k T})^{-\frac{1}{2}} \tag{2.10}$$

where σ_m is the conductivity of the liquid medium, z is the valence of the ion, e is the elementary charge, μ_m is the bulk ion mobility, k is Boltzmann's constant and T is the temperature. The relationship is shown in **Fig.2.2**(**a**).

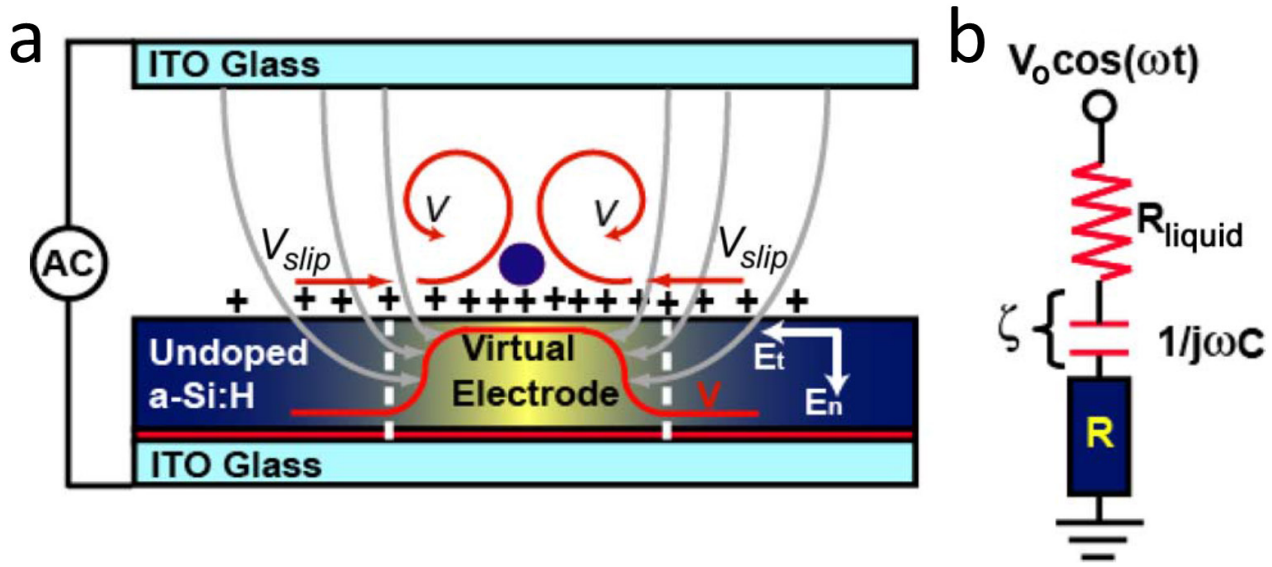

Figure 2.1: (**a**) Working principle of LACE in OET. (**b**) The equivalent circuit model of LACE. Figure reproduced with permission from: **a-b**,ref.[35] ©2008 IEEE.

The existence of the EDL (capacitor) determines the frequency-dependent LACE. A too high frequency will cause a too low impedance of the EDL capacitor and the domination of the liquid medium resistor, resulting in a small zeta potential ζ and a small slip velocity ν_{SLIP}. A too low frequency will cause a too high impedance of the EDL capacitor and a small electrical potential across the EDL, resulting in a small tangential component of electric field as well as a small slip velocity ν_{SLIP}. In order to reach the maximum zeta potential ζ in **Eq.(2.9)**, an optimal AC frequency f_{opt} can be estimated to be[35]:

$$f_{opt} = \frac{\sigma_m d}{2\pi\varepsilon L} \tag{2.11}$$

where L is the gap spacing of the liquid layer. **Fig.2.2(b)** shows the relationship between the maximum slip velocity ν_{SLIP} and the AC frequency.

A KCL solution is used as the liquid medium to generate experimental data in **Fig.2.2**. The bulk ion mobility μ_m is 8×10^{-8} $m^2V^{-1}s^{-1}$, the valence of the ion z is 1, the conductivity σ_m is assumed as $\sigma_m = e\mu_m n^0$ where n^0 is the bulk ion concentration. At frequency below 1 kHz, LACE will be the dominant effect[54].

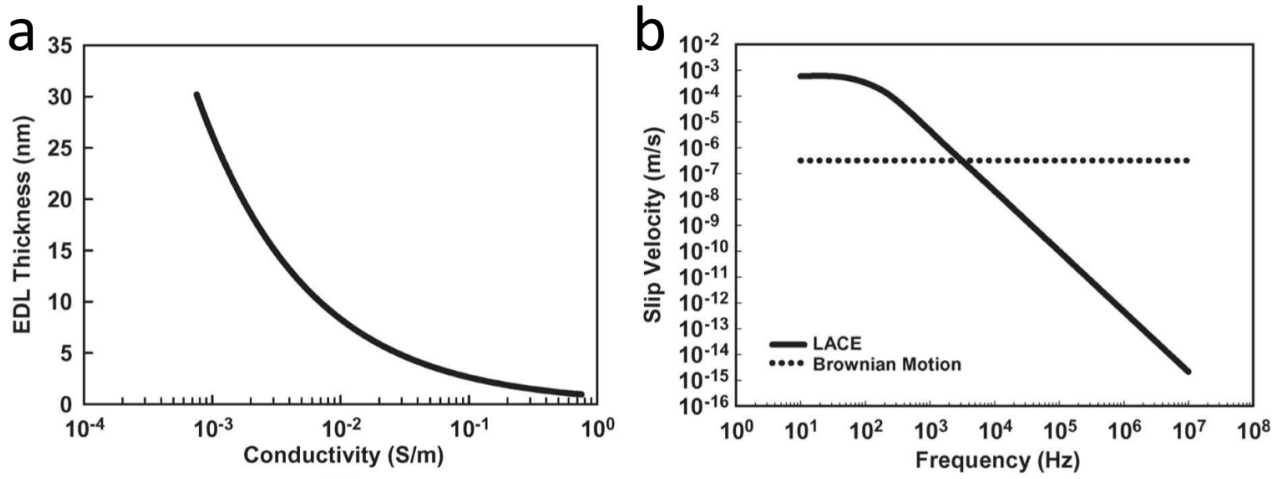

Figure 2.2: (**a**) The dependence of the EDL thickness d on liquid conductivity σ_m. (**b**) The dependence of the maximum slip velocity ν_{SLIP} on the AC frequency at 1 kHz and 20 V_{pp} with an optical power density of 250 W/cm^2. A dot line depicts the travel distance of a 10 μm particle in 1 s due to Brownian motion. Figure reproduced with permission from: **a-b**,ref.[54] ©2008 IEEE.

2.1.3 Electrothermal (ET) Effect

The incident light will create not only LIDEP and LACE, but also electrothermal (ET) effect. The photons absorption at the photoconductive layer is dissipated through either the electron-hole pair or phonon generation which forms a localized heat source at the photoconductive layer. In addition, the applied electrical potential caused heating in the liquid medium and at the photoconductive layer can be calculated as[54]:

$$W = \sigma_m E^2 \tag{2.12}$$

where W is the power generated per unit volume, σ_m is the conductivity of the surrounding medium and E is the applied electrical potential. In the liquid medium, a gradient in electrical permittivity and conductivity is caused by the generated heat so that a body force is produced. The time-averaged body force per unit volume can be described as[36]:

$$< f_{ET} >= \frac{1}{2} Re[(\frac{\sigma_m \varepsilon}{\sigma_m + i\omega\varepsilon}(\kappa_\varepsilon - \kappa_\sigma))(\Delta T \times E)E^*] - \frac{1}{2}|E|^2 \kappa_\varepsilon \varepsilon \Delta T \tag{2.13}$$

where κ_σ and κ_ε are the empirical constants of the percent change per unit temperature in conductivity and electrical permittivity. In typical electrolytes, κ_σ=2%K^{-1} and κ_ε=-0.4%K^{-1}[36].

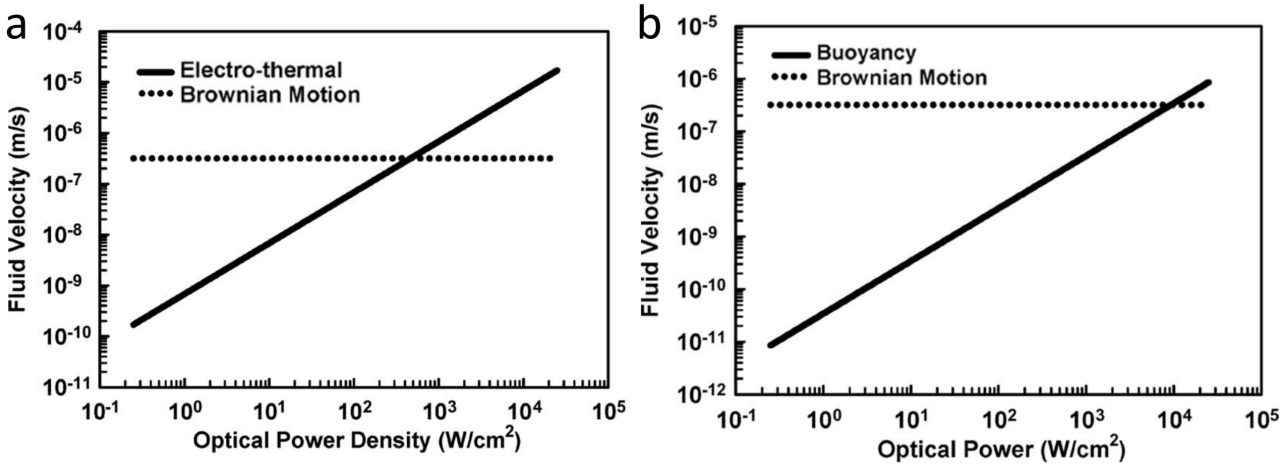

Figure 2.3: At the condition of 100 kHz and 20 V_{pp}, (**a**) the dependence of the ET fluid velocity on incident optical power density and (**b**) the dependence of the buoyancy fluid velocity on the optical power density. A dotted line depicts the travel distance of a 10 μm particle in 1 s due to Brownian motion. Figure reproduced with permission from: **a-b**,ref.[54] ©2008 IEEE.

Fig.2.3(**a**) shows that the ET caused fluid velocity is directly proportional to the optical power density. At high optical power density, a high temperature gradient and high electric field will lead to the domination of ET in OET device.

2.1.4 Buoyancy Effect

The liquid medium can exert an upward force that opposes the weight of the immersed particles. The localized temperature gradient will lead to a fluid density gradient since the fluid density is a function of temperature. The fluid density gradient will influenced by gravity so that a fluid flow is formed, which can be characterized by[64]:

$$f_G = \frac{\partial \rho_m}{\partial T} \Delta T \times g \tag{2.14}$$

where ρ_m is the fluid density, T is temperature and g is the gravitational acceleration.

Fig.2.3(**b**) shows that the buoyancy driven fluid flow is not comparable to Brownian motion until a high optical power density (10^4 W/cm^2) is reached. In addition, the magnitude of the fluid flow caused by buoyancy is much less than other effects. **Fig.2.4** demonstrates that the simulated fluid flow patterns due to each effect, in which the buoyancy driven fluid flow (**Fig.2.4**(**c**)) has a reverse direction to both LACE (**Fig.2.4**(**a**)) and ET (**Fig.2.4**(**b**)). Unless there is no applied electrical potential, the buoyancy will not play an important role in OET.

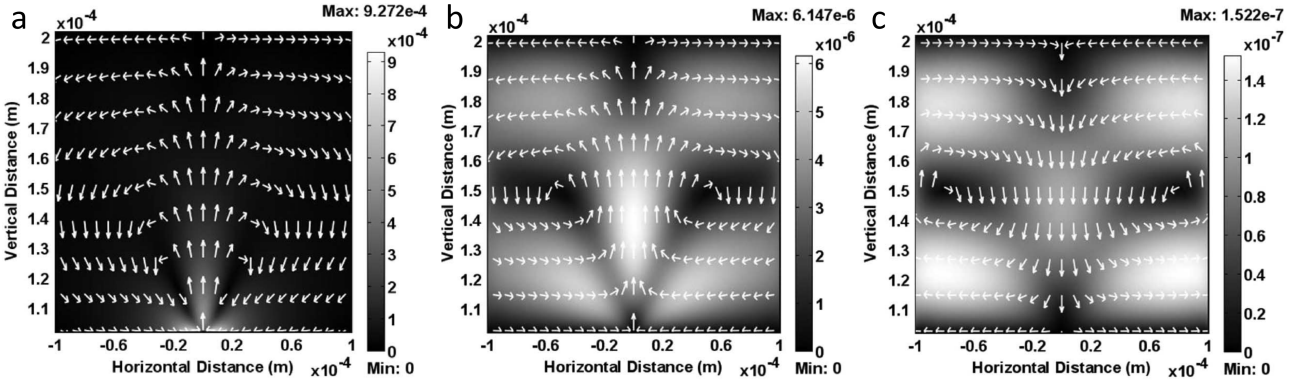

Figure 2.4: At the condition of 100 kHz and 20 V_{pp} with 250 W/cm^2 optical power density, the simulated fluid flow patterns due to (**a**) LACE, (**b**) ET and (**c**) buoyancy. Figure reproduced with permission from: **a-c**,ref.[54] ©2008 IEEE.

2.1.5 Figure of Merit

As a multitude of physical regimes are presented in the OET device, it is necessary to use a figure of merit to determine the dominant effect at a certain condition. Based on the velocity of fluid and particle, Justin K. Valley et al. first defined a dimensionless value β as[54]:

$$\beta \equiv \frac{X_{DEP}}{X_{DEP} + X_{EXT} + < X_{BROWNIAN} >} \tag{2.15}$$

where the symbol X is defined as the travel distance of a particle in 1 s under a certain force. DEP, EXT and $BROWNIAN$ refer to the force exerted by DEP, external (LACE, ET, buoyancy) and Brownian motion, respectively. The average travel distance of a particle in 1 s due to Brownian motion can be characterized by the following[65]:

$$< X_{BROWNIAN} >= \sqrt{\frac{kT}{3\pi\eta r}} \tag{2.16}$$

If the dimensionless value β is applied over an area, a new figure of merit B is obtained[50],[54]:

$$B \equiv \frac{1}{A}\int_A \beta dxdy, x \in [-r, r], y \in [0, d] \tag{2.17}$$

where r is the maximum radius from the centre of the optical pattern that particle perturbation is expected, d is the liquid chamber thickness and A is the integration area that equals to $2\times r\times d$. B refers to the average value of β therefore has the value between 0 and 1.

In OET device, there are three main physical regimes including DEP, LACE and ET. For a given set of parameters such as optical power density and frequency, the dominant operational effect in OET device can be interpreted. Experimental results with theoretical predictions explain the dominant effect as a function of optical power density and frequency (**Fig.2.5**(**a**)-(**b**)). **Fig.2.5**(**c**) shows that LACE is the dominant effect at a low frequency (below 1 kHz), ET is the dominant effect at a high optical power density and DEP is the dominant effect at a typical OET operating parameters.

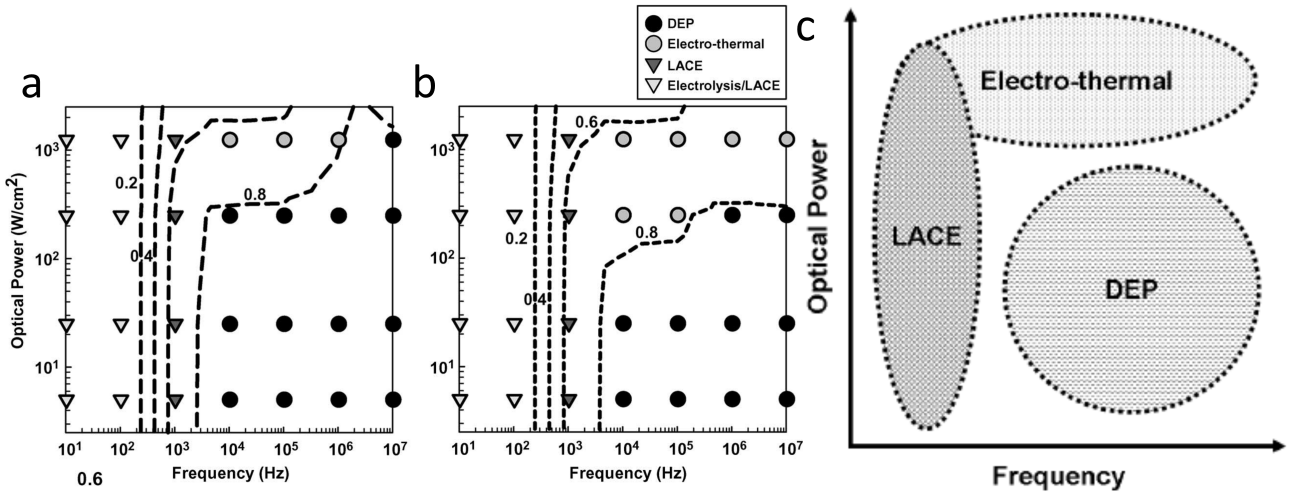

Figure 2.5: Experimental results with theoretical predictions of the dominant effect. Experimental data produced at the condition of 100 kHz and 1 mS/m conductivity at (**a**) 20 V_{pp} and (**b**) 10 V_{pp}. Dashed lines on (**a**)-(**b**) depict the theoretical simulations. (**c**) Physical regimes as a function of optical power density and frequency in OET. Figure reproduced with permission from: **a-b**,ref.[54] ©2008 IEEE; **c**,ref.[32], ©2009 Arash Jamshidi.

DEP therefore is the dominant operational effect under our experimental conditions (25 V_{pp}, 15 kHz frequency).

2.2 Photoconductive Materials

The use of photoconductive materials plays an important role in creating the virtual electrodes in OET. A typical OET structure consists of a liquid solution chamber sandwiched between a top indium tin oxide (ITO) coated glass electrode and a bottom photosensitive electrode with an applied AC voltage between these two electrodes (**Fig.2.6**(**a**)). The incident light will generate charge carriers, resulting in a rapidly increasing (a few orders of magnitude) conductivity at the illuminated area in photoconductive material. Therefore, at the illuminated area, the photosensitive electrode will have a low conductivity dark state without illumination and a high conductivity illuminated state with illumination. A simplified equivalent circuit model (**Fig.2.6**(**b**)) can be used to explain these states. At the dark state, the impedance of the photosensitive electrode Z_{PC} is greater than the impedance of the liquid solution Z_L so that most of the applied AC voltage will drop across the photosensitive electrode. At the illuminated state, Z_{PC} is much lower than Z_L therefore a significant voltage drop at the liquid

solution forms the electric field gradient. The formation of the two states allows an optically defined virtual electrode to produce LIDEP. The resolution of these virtual electrodes depends on photoconductive materials, illuminated conductivity and optical patterns[25],[66].

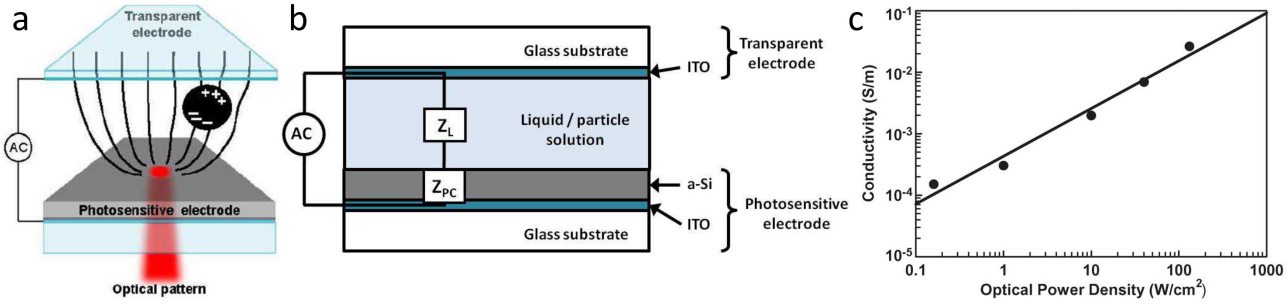

Figure 2.6: (**a**) A typical OET structure. (**b**) The simplified equivalent circuit model of OET. (**c**) Experimental a-Si:H conductivity versus optical power density. Figure reproduced with permission from: **a-b**,ref.[50] ©2010 IN TECH; **c**,ref.[54] ©2008 IEEE.

Hydrogenated amorphous silicon (a-Si:H) is an ideal material for photosensitive electrode in OET devices. The photoconductivity of a-Si:H is shown in (**Fig.2.6**(**c**)), which exhibits high resistance at a low optical power density and high conductance at a high optical power density. In other words, a-Si:H has a low conductivity dark state as well as a high conductivity illuminated state to form the virtual electrodes.

OET devices have also been constructed from other alternate photosensitive materials such as P3HT:PCBM[67], titanium oxide phthalocyanine[68] and cadmium sulphide (CdS)[69].

Chapter 3

Experimental Techniques and Results

3.1 Experimental Preparation

Figure 3.1: (**a**) Olympus UC30 Microscope Digital Cameras. ref.[70] (**b**) Olympus BX51. ref.[71] (**c**) ProScan II H101A stage. ref.[72] (**d**) Dell 1510X Projector. ref.[73] (**e**) ProScan III H31 Automation Controller. ref.[74] (**f**) Proscan III PS3J100 Interactive control Centre. ref.[75] (**g**) ISO TECH IPS 2303D laboratory DC power supply. ref.[76] (**h**) TTi TG5011 50MHz function/arbitrary/pulse generator. ref.[77] (**i**) TTi WA301 Wideband 30V pk-pk amplifier for waveform generation. ref.[78] (**j**) Cole-Parmer StableTemp Hot Plates. ref.[79] (**k**) Keysight B1500A Semiconductor Device Analyzer. ref.[80] (**l**) Thermo Scientific Heraeus PowerDry LL3000 Freeze drying systems. ref.[81] (**m**) CascadeMicrotech MPS150 Manual Probe System. ref.[82] (**n**) Hitachi S-4700 SEM. ref.[83] (**o**) SUSS MicroTec MA6. ref.[84]

3.1.1 Sample Preparation

Four types of micro- and nanoscale objects have been used in this experiment including micro-light-emitting diode (micro-LED), carbon nanotubes (CNTs) (SIGMA-ALDRICH, 724777), solder beads (IPS Solder Powders, Leaded alloys) and silver-coated PMMA microspheres (Cospheric, PMPMSAG-1.53).

Each micro-LED has the size of 100 × 100 μm and consists of both n-type GaN, InGaN/GaN quantum wells and p-type GaN. Metal electrodes are fabricated on both sides of these micro-LEDs[85]. The CNTs we used have the diameter ranging from 0.7 nm to 1.4 nm with a bulk density of 0.091 g/mL. The alloy composition of solder beads we used is $Sn_{62}Pb_{35.6}Ag_2$ with a melting point of 179 °C. These solder beads have the size ranging from 25 μm to 45 μm. The silver-coated PMMA microspheres have the size ranging from 45 μm to 53 μm. The thickness of the coated silver layer is around 250 nm.

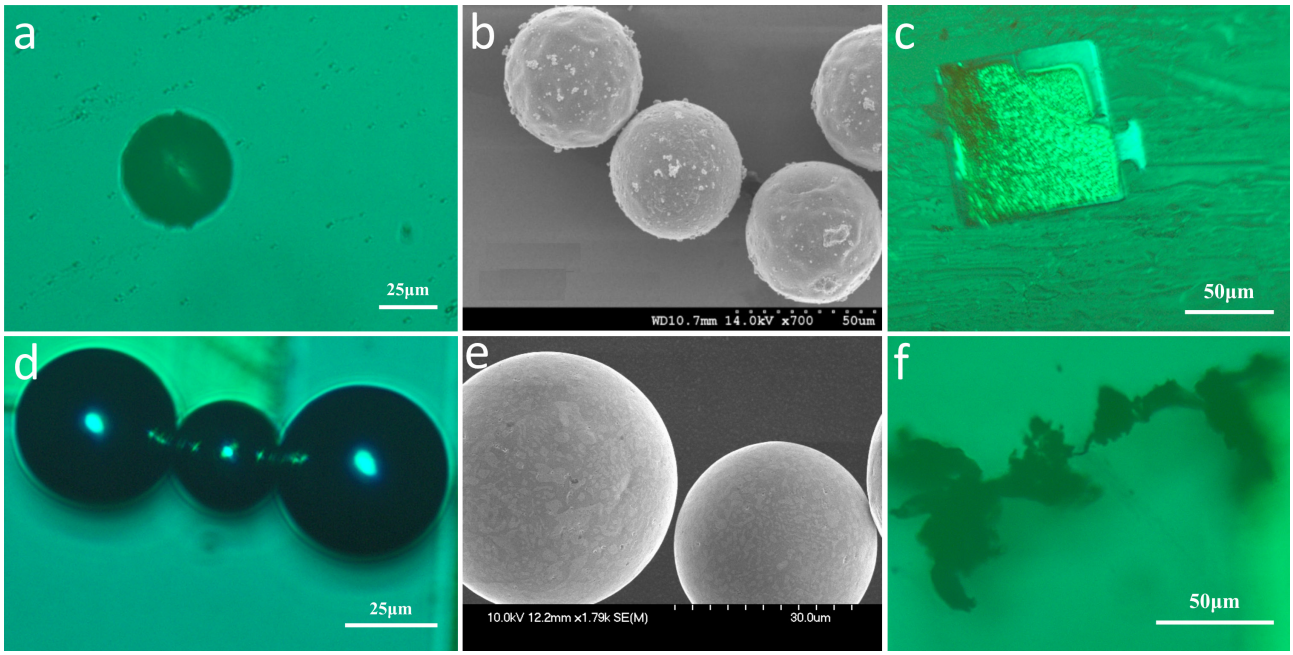

Figure 3.2: (**a**)-(**b**) Silver-coated PMMA microspheres. (**c**) A GaN micro-LED. (**d**)-(**e**) Solder beads. (**f**) Carbon nanotubes.

In order to make the sample suitable for the OET experiment, all of these micro- and nanoscale objects were added into a liquid solution, separately. Non-ionic surfactant (TWEEN 20, SIGMA P9416) has been added into deionized water solvent with concentration of 0.05% so that the liquid solution can have a better conductivity and minimize the clumps of particles.

3.1.2 Device Fabrication

The OET device we used in this experiment has a sandwich structure, a liquid chamber contained micro-objects is sandwiched between a top electrode and a bottom electrode with an applied AC potential on both electrodes. The top electrode made up of indium tin oxide (ITO) coated glass slide (Diamond Coatings, UK) while the bottom electrode consists of photosensitive layer and metal electrodes. Hydrogenated amorphous silicon (a-Si:H) is used for the photosensitive material which is deposited on a ITO coated glass slide by plasma-enhanced chemical vapor deposition (PECVD) with thickness of 1 μm at 300 °C. A SiO_2 layer with thickness of 350 nm is coated on the top of the a-Si:H in order to prevent the conducting between the metal electrode and the photosensitive later. After a series of photolithography (SUSS MicroTec MA6, **Fig.3.1(o)**) process including spin, bake, exposure, develop, etching and lift-off together with electron-beam evaporator (Plassys IV), defined metal electrodes have been deposited on the top of the SiO_2 and the rest of the a-Si:H layer is exposed by reactive-ion etching (RIE). **Fig.3.3** shows the whole fabrication process of the bottom electrode.

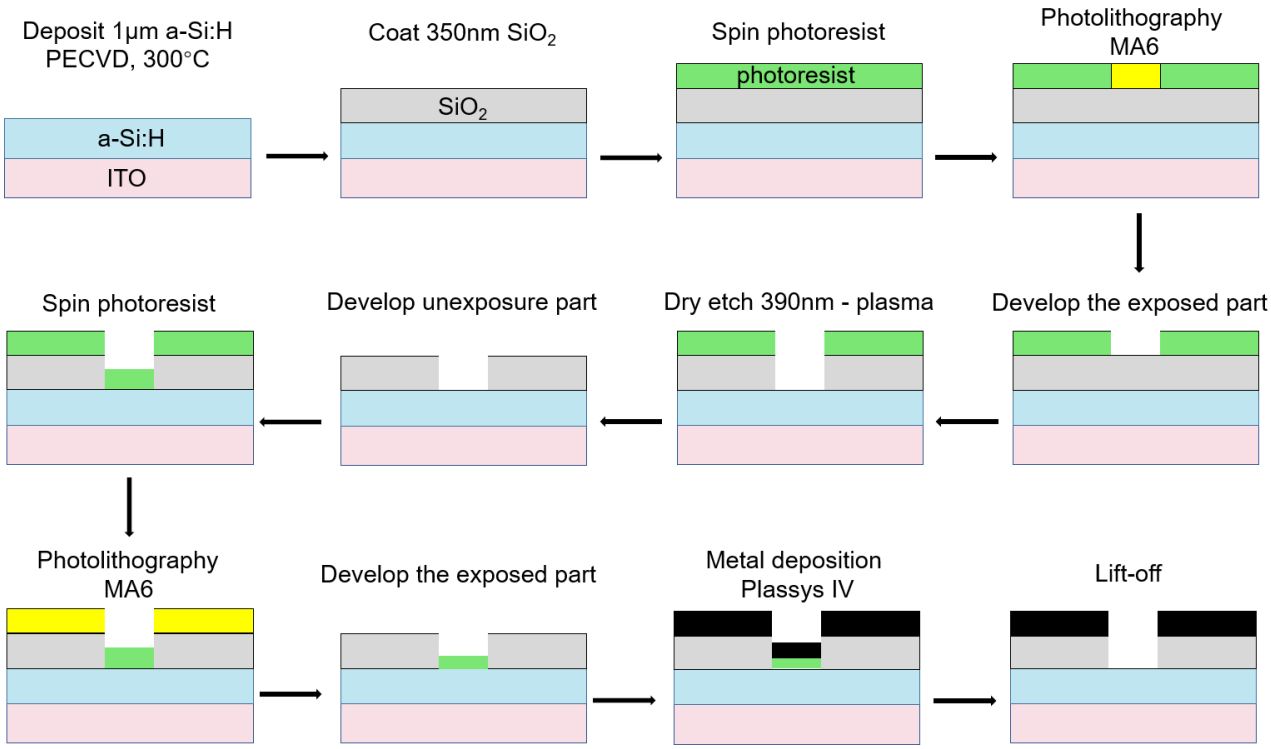

Figure 3.3: The fabrication process of the bottom electrode.

The OET device we used is shown in **Fig.3.4**. ITO and a-Si:H are cut into a desirable size. Normal conducting wires are fixed on each electrode by silver epoxy and waterproof glue (**Fig.3.4**(**a**)). Since the assembly of solder conducting path needs a melt process, a removable conductive tape is used to fix the normal conducting wire (**Fig.3.4**(**b**)). Otherwise, these glues will melt and destroy the whole sample. Waterproof tape with thickness of 100 μm is used to merge the top and bottom electrodes into a OET device (**Fig.3.4**(**c**)-(**d**)). Therefore, the liquid chamber has the thickness of 100 μm as well.

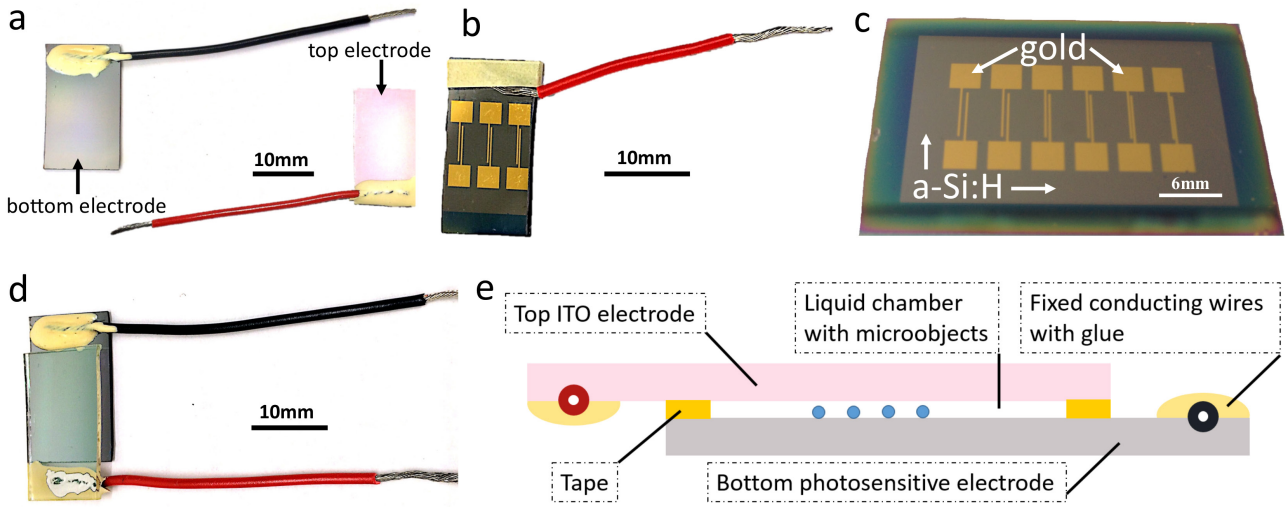

Figure 3.4: (**a**) The bottom photosensitive electrode (left, with black wire) and the top ITO electrode (right, with red wire). The bottom photosensitive electrode with metal electrodes (**b**) after and (**c**) before cutting into a desirable size. (**d**) Image and (**e**) schematic diagram of the OET device.

3.1.3 Experimental Setup

A commercial data projector (Dell 1510X, **Fig.3.1**(**d**)) acts as the light source. The light is introduced into an optical microscope (Olympus BX51, **Fig.3.1**(**b**)) and illuminating on the OET device with an incident direction from top to bottom. The reason a conventional bottom to top incident direction is not used in our experiment is that the photosensitive layer can absorb most of the light resulting in a poor visibility during manipulation. The shape of the illuminated area is freely defined by the computer since a computer can easily change the projection area of a data projector. A microscope digital camera (Olympus UC30, **Fig.3.1**(**a**)) on top of the optical microscope is used to record images and videos during the experiment. Optical filters

have been used in the optical path including a long pass filter (Thorlabs FD1R) that attenuates blue light from the data projector and a short pass filter (Thorlabs FES0550) that attenuates red light so that the recorded images can be distinguished easily. The OET device is put on the top of a motorised stage (ProScan II H101A, **Fig.3.1**(**c**)) which can be controlled manually or automatically. The applied AC potential between top and bottom electrodes of the OET device is generated by a function generator (TTi TG5011, **Fig.3.1**(**h**)) together with an amplifier (TTi WA301, **Fig.3.1**(**i**)). The output Sine AC current is set to 15 kHz frequency and 25 V_{pp}.

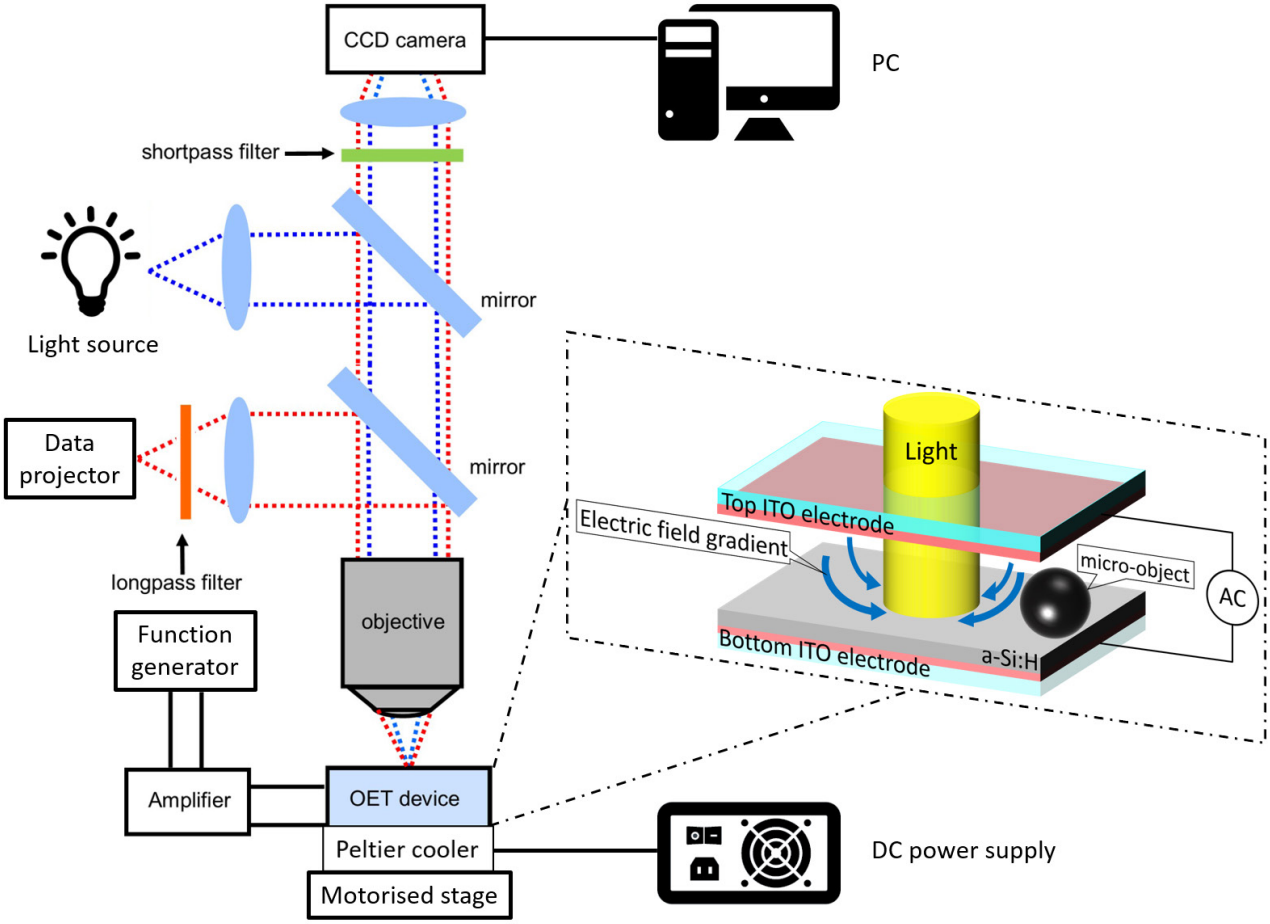

Figure 3.5: Schematic diagram of experimental setup and OET device.

3.1.4 Demonstration Experiments

After the experimental setup, some demonstration experiments (**Fig.3.6**) can be used to check the working condition of OET device. The solder beads are successfully trapped by the light patterns (**Fig.3.6**(**a**)-(**c**)), which shows a strong positive DEP force. **Fig.3.6**(**d**) demonstrates

the characteristic of parallel manipulation for OET.

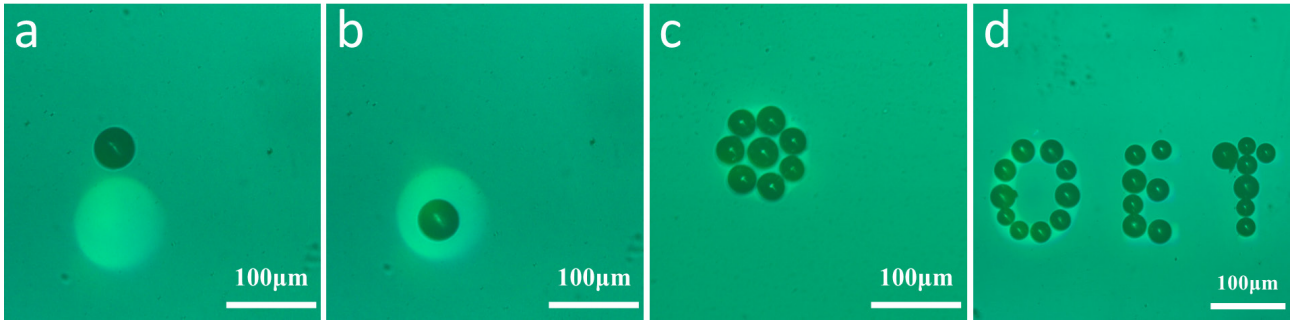

Figure 3.6: Optical microscope images of a solder bead (**a**) before and (**b**) after being trapped by a circular light pattern; (**c**) Eight solder beads trapped by a circular light pattern; (**d**) 'OET' formed by assembling solder beads via OET device.

3.2 Distribution after Random Movement

The purpose of using OET to assemble solder beads is to build conducting path, which is the prerequisite of SMT. Solder beads should have a tight connection between each other after assembling so that a good electrical connection can be built after a melt process. Therefore, how precise can the mounting be done by OET becomes a significant factor. By setting up a series of experiments about random movement, this factor can be investigated. We first use OET to trap a 45 μm diameter solder bead to a clear area and set this position as the coordinate origin. Then, this solder bead is dragged by OET to a series of random coordinate points, separately. For each movement, a series of coordinate points have been recorded in **Table 3.1**, then the displacement can be measured (**Fig.3.7**).

Table 3.1: Centre coordinates of light patterns and solder beads.

light pattern	solder bead
(a_i, b_i)	(p_i, q_i)

where i is the group number of experiment.

The solder bead displacement (x, y) is given by the centre-to-centre distance between solder bead and light pattern:

$$(x, y) = (a_i - p_i, b_i - q_i) \tag{3.1}$$

Fig.3.7 gives an example of how to measure the centre-to-centre distance between solder bead and light pattern.

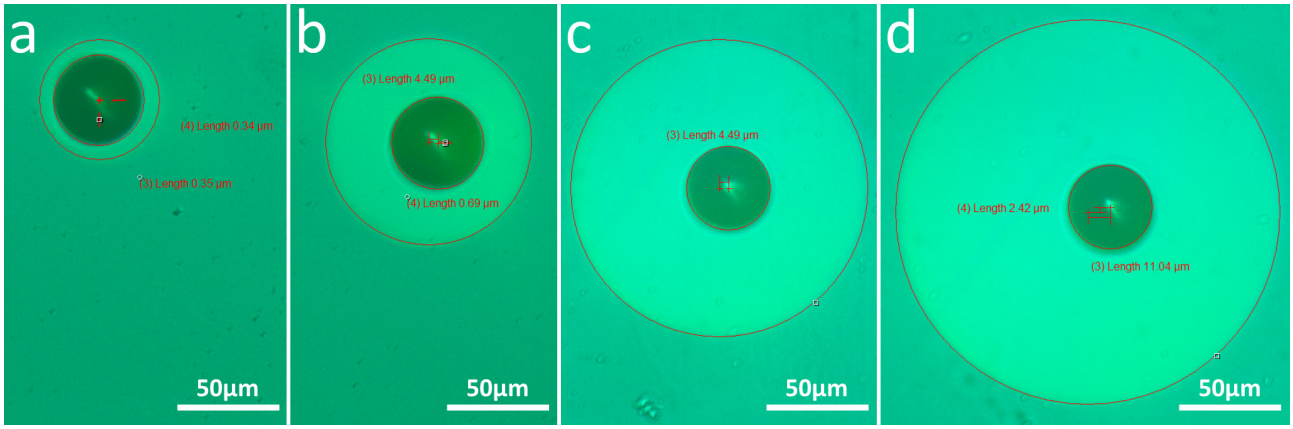

Figure 3.7: Optical microscope images of a 45 μm solder bead trapped by (**a**) 60 μm, (**b**) 100 μm, (**c**) 150 μm and (**d**) 200 μm diameter circular light patterns with the displacement of (**a**) (-0.35μm, -0.34μm), (**b**) (4.49μm, -0.69μm), (**c**) (4.49μm, 0μm) and (**d**) (11.04μm, 2.42μm).

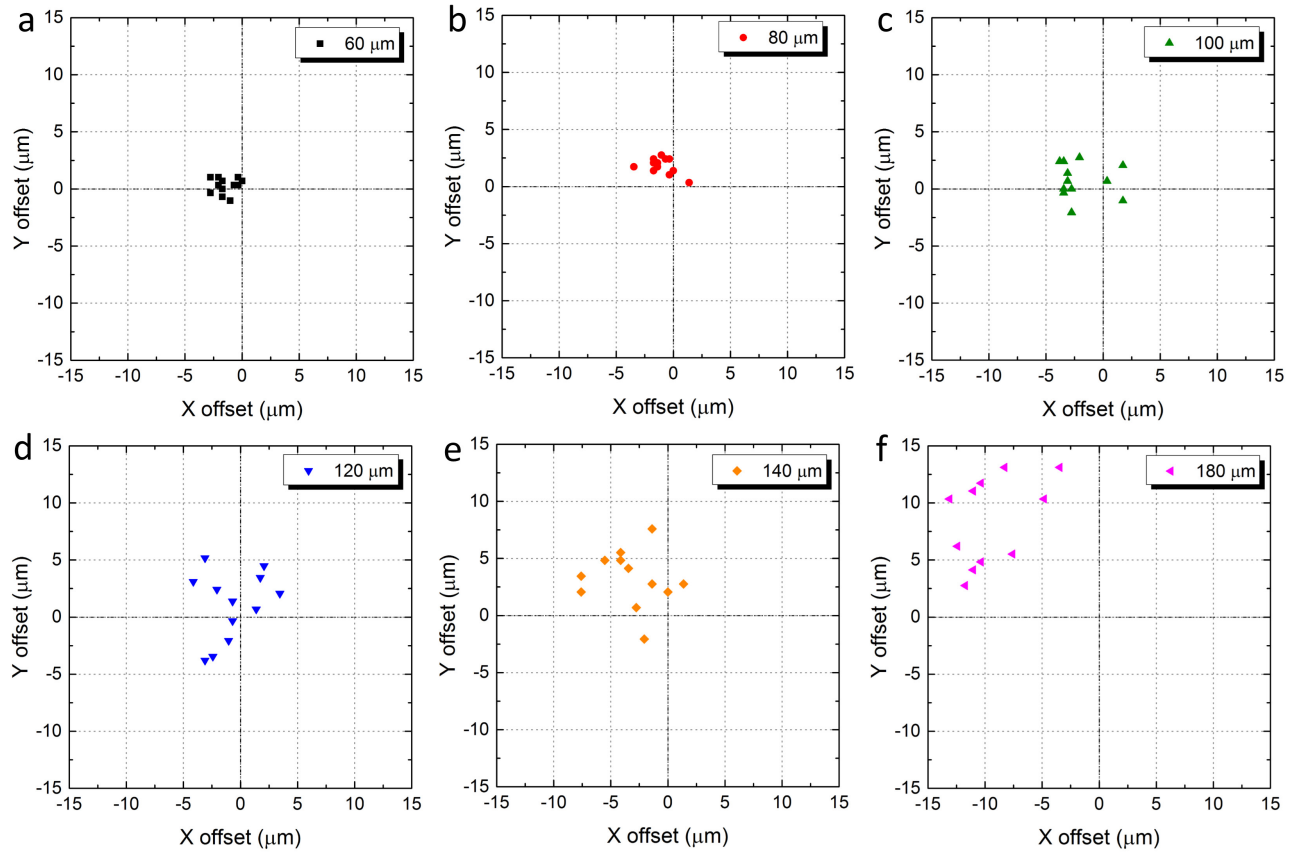

Figure 3.8: Distribution of a 45 μm solder beads trapped by (**a**) 60 μm, (**b**) 80 μm, (**c**) 100 μm, (**d**) 120 μm, (**e**) 140 μm and (**f**) 180 μm diameter circular light patterns.

After random movement, these displacements can be used to generate the graph of distribution (**Fig.3.8**) which shows a trend that the distribution of solder beads become more discrete as

the diameter of light pattern increases. In other words, a larger light pattern may lead to a more unpredictable position of the solder beads.

The full range of data used to calculate the displacements and determine the distribution of the 45 μm solder beads is shown in **Appendix A.1**.

Theoretically, solder beads should have equal opportunities to distribute in all directions due to the symmetry of circular light pattern. In other words, the distribution of solder beads should concentrate on the coordinate origin. However, non-uniform light intensity in light patterns may lead to an non-uniform distribution of solder beads. In order to offset this error and plot the graph more ideally, all of the points should be moved to a certain distance which equals to the average displacement value. After non-uniform offset, **Fig.3.9** shows a clearer trend to support the inference - a larger light pattern will lead to a more unpredictable position of solder beads in OET micro-manipulation.

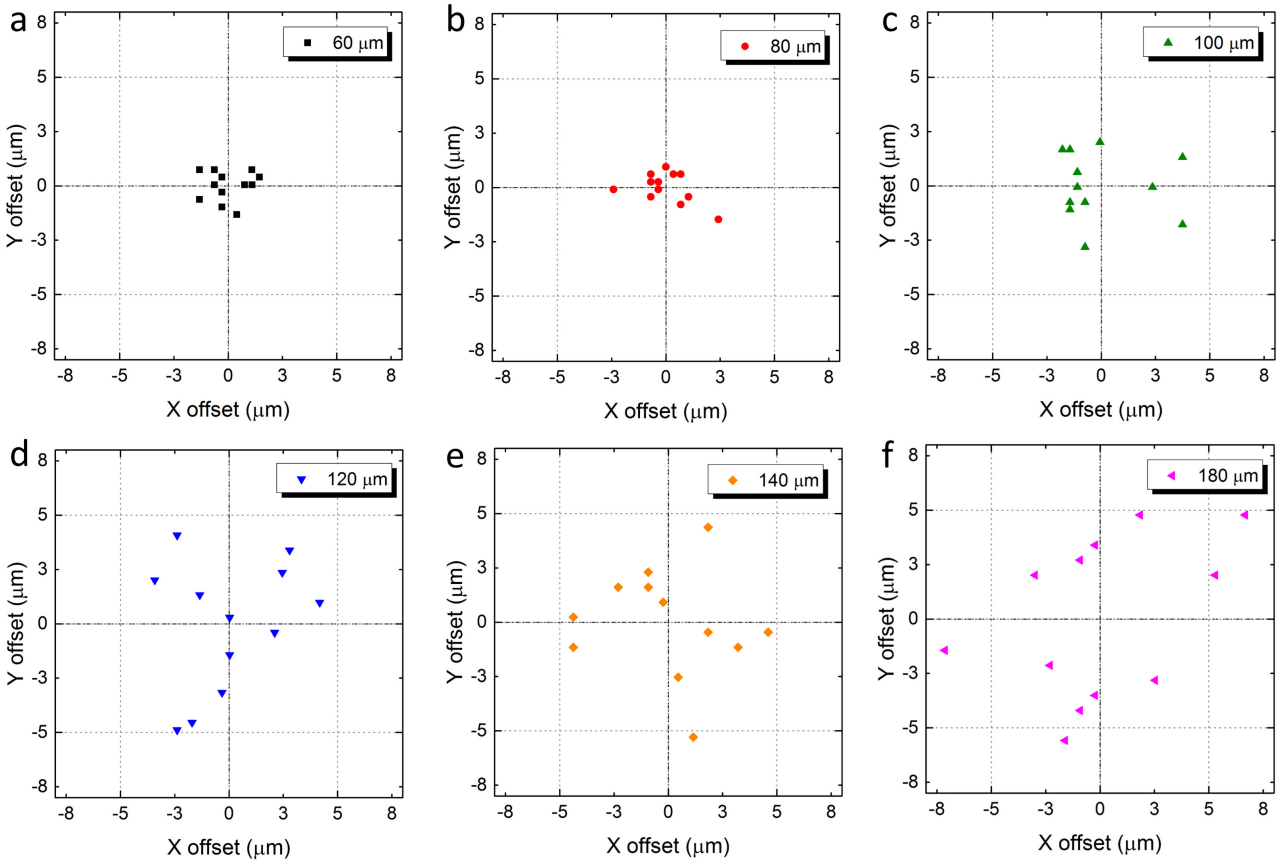

Figure 3.9: Distribution of the solder beads after non-uniform offset.

The same experimental procedure has been used in the 50 μm silver-coated PMMA microspheres to verify this inference. **Fig.3.10** shows a similar result as the solder beads, which reveals the relationship between the position and the size of OET light pattern.

The full range of data used to calculate the displacements and determine the distribution of the 50 μm silver-coated PMMA microspheres is shown in **Appendix B.1**.

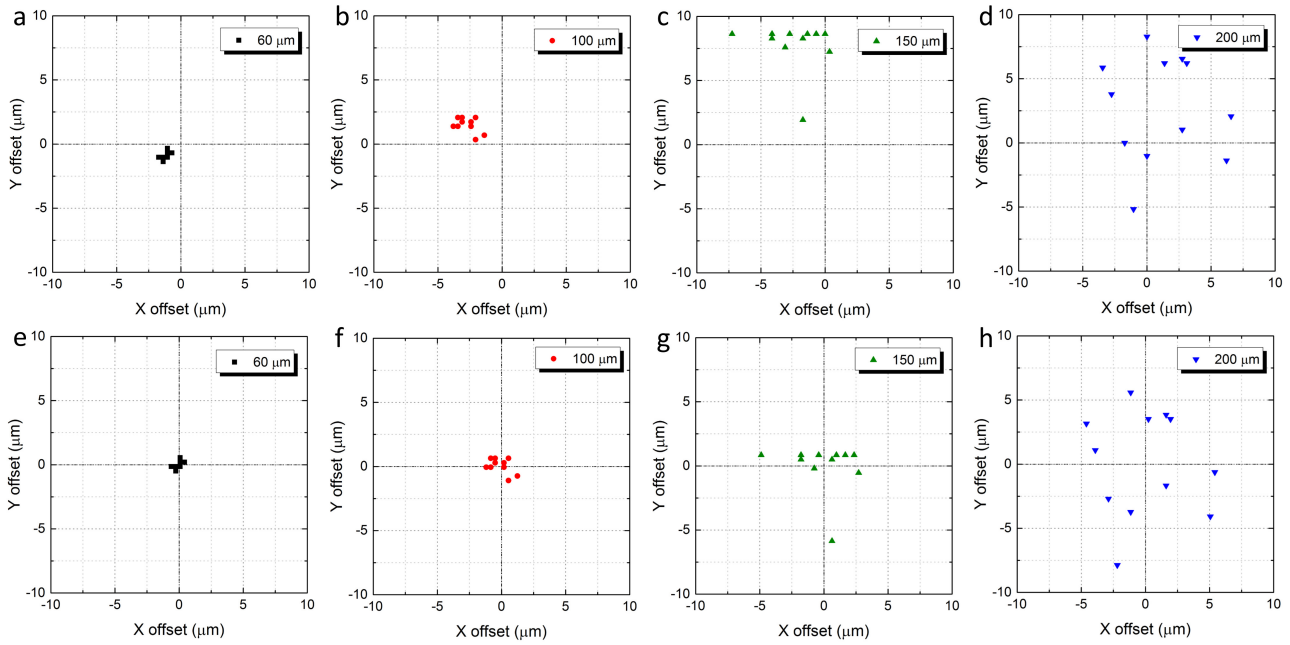

Figure 3.10: Distribution of the 50 μm silver-coated PMMA microspheres trapped by (**a**) 60 μm, (**b**) 100 μm, (**c**) 150 μm and (**d**) 200 μm diameter circular light patterns, after random movement. (**e**)-(**f**) Distribution of the silver-coated PMMA microspheres after non-uniform offset.

This inference can be used as a guide for choosing an appropriate diameter of light pattern in the OET based SMT to achieve a higher accuracy.

3.3 Investigation into Accuracy

The distribution of solder beads and silver-coated PMMA microspheres after random movement shows a basic relationship between the accuracy and the diameter of light pattern. However, displacements can only be used as a qualitative analysis. It is hard to quantify accuracy based on distribution. The average displacement has the physical meaning of the actual centre of distribution. More importantly, it cannot avoid accidental situation. For example, the average displacement of (-10μm, -5μm) and (10μm, 5μm) is (0, 0) which cannot reveal the great value changes. For a further investigation of the accuracy in different diameter light patterns, a relative values can be used to defined the accuracy.

Here, we propose a definition of accuracy in X-axis and Y-axis directions as:

$$X = \frac{\sum_{i=1}^{n} |(a_{i+1} - a_i) - (p_{i+1} - p_i)|}{n-1}, \; Y = \frac{\sum_{i=1}^{n} |(b_{i+1} - b_i) - (q_{i+1} - q_i)|}{n-1} \tag{3.2}$$

where n is the natural number and i is the group number of experiment.

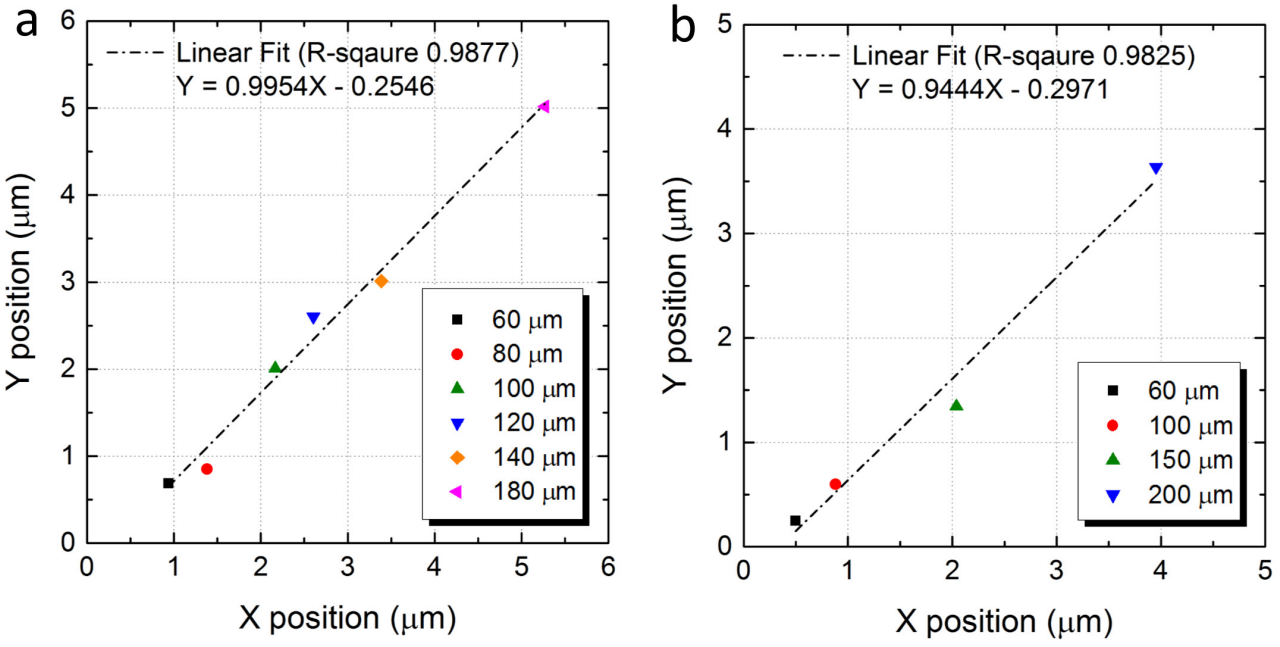

Figure 3.11: Accuracy in X-axis and Y-axis directions of (**a**) the 45 μm solder beads and (**b**) the 50 μm silver-coated PMMA microspheres with different diameter circular light patterns.

The full range of data for accuracy of the 45 μm solder beads and the 50 μm silver-coated PMMA microspheres are shown in **Appendix A.1** and **Appendix B.1**, separately.

Theoretically, the accuracy in X-axis direction should equal to the accuracy in Y-axis direction due to the symmetry of circular light pattern.

$$Y = X \tag{3.3}$$

The accuracy in X-axis and Y-axis directions of the 45 μm solder beads is well described by the linear fit $Y = 0.9954X - 0.2546$ (dash dot line) with $R^2 = 0.9877$ in **Fig.3.11**(**a**). The linear fit comes very close to the experimental expectation (**Eq.**(**3.3**)). The accuracy of the 50 μm silver-coated PMMA microspheres has been measured in order to verify the theoretical prediction as well. **Fig.3.11**(**b**) indicates the linear fit $Y = 0.9444X - 0.2971$ (dash dot line) with $R^2 = 0.9825$.

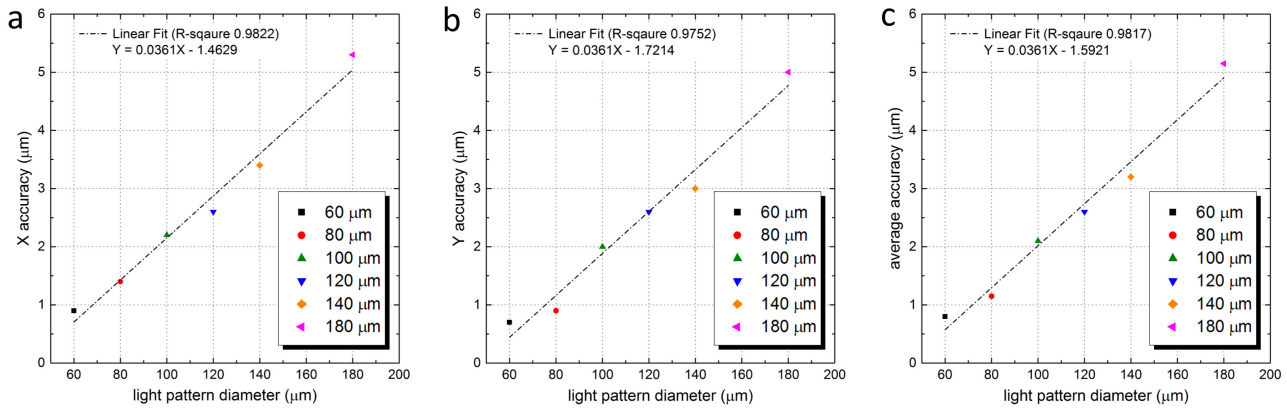

Figure 3.12: (**a**) X-axis direction, (**b**) Y-axis direction and (**c**) average accuracy of the 45 μm solder beads with different diameter circular light patterns.

Fig.3.12 shows a linear relationship between the accuracy and the diameter of light patterns under 180 μm. All the three linear fits have the slope of 0.0361 and the R^2 very approximately equals to 1.

The highest accuracy we achieved is 0.8 $\pm$ 0.1 μm with 60 μm diameter light pattern for 45 μm solder beads.

The investigation into distribution and accuracy indicates a way to choose an appropriate light pattern size in assembling.

3.4 Dielectrophoresis Force and Trap Profiles

According to the Stokes' law with Faxen's correction (**Eq.2.6-2.8**), the trapping speed of the solder beads can be used to calculate the DEP force. The relative speed of solder bead and light pattern can be controlled by the motorised stage (ProScan II H101A, **Fig.3.1**(**c**)). First we gradually increase the speed until the trapped solder bead escapes from the trap so that the maximum trapping speed is determined (2800 μm/s). We then vary the speed from maximum trapping speed down to 100 μm/s and measure the centre-to-centre distance between solder bead and light pattern.

Fig.3.13 demonstrates how we measure the centre-to-centre distance more accurately. The displacements which previously mentioned have to be taken into consideration. Therefore, the static displacements before dragging is first measured (**Fig.3.13**(**a**)). Additionally, at a specific speed, five frames during dragging are used to calculate the average centre-to-centre distance and the standard deviation (error bars). **Fig.3.13**(**b**)-(**d**) show three frames during dragging by a 140 μm diameter circular light pattern at 2500 μm/s from which a different centre-to-centre distance can be seen in each frame.

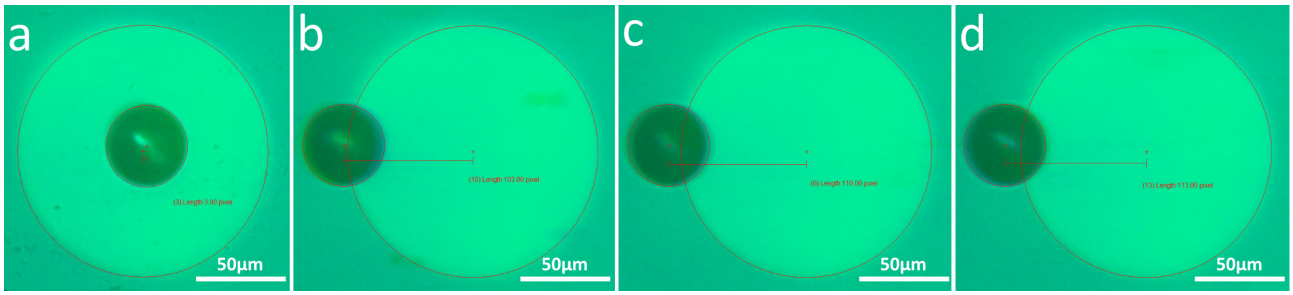

Figure 3.13: Optical microscope images of a 45 μm solder bead (**a**) before and (**b**)-(**d**) during dragging by a 140 μm diameter circular light pattern at 2500 μm/s. These centre-to-centre distance between solder bead and light pattern are (**a**) +2.16 μm (3 pixels), (**b**) -74.16 μm (103 pixels), (**c**) -79.2 μm (110 pixels) and (**d**) -81.36 μm (113 pixels).

Fig.3.14 shows some snapshots of solder beads trapped by different diameter light patterns at different speed. It can be found that a higher speed will lead to a greater centre-to-centre distance, which qualitatively confirms solder bead will experience a larger DEP force at the edge of the trap.

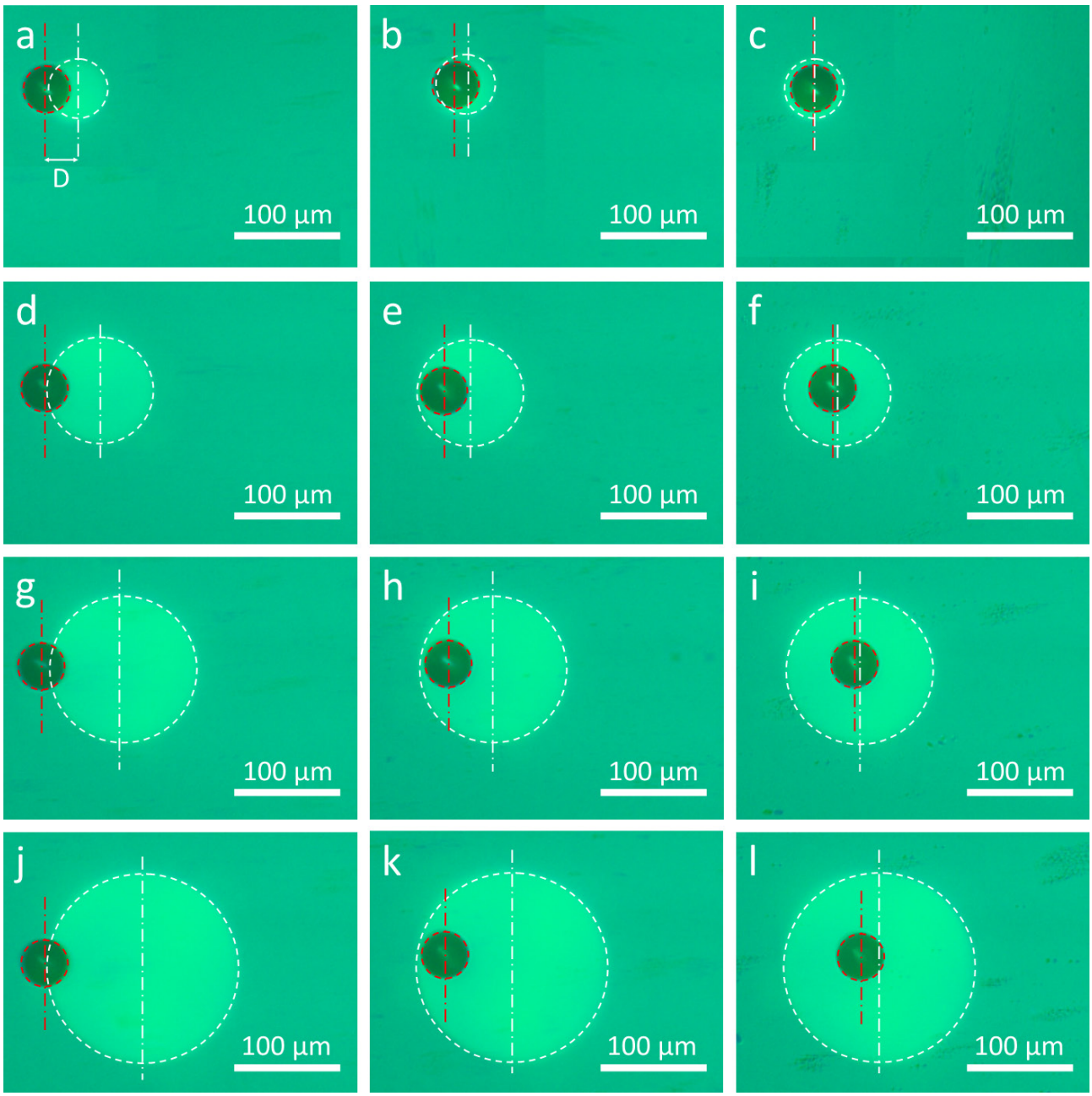

Figure 3.14: Optical microscope images of a 45 μm solder bead trapped by 60 μm diameter circular light pattern at (**a**) 2500 μm/s, (**b**) 1200 μm/s and (**c**) 100 μm/s; 100 μm diameter circular light pattern at (**d**) 2800 μm/s, (**e**) 1200 μm/s and (**f**) 100 μm/s; 140 μm diameter circular light pattern at (**g**) 2500 μm/s, (**h**) 1200 μm/s and (**i**) 100 μm/s; and 180 μm diameter circular light pattern at (**j**) 2500 μm/s, (**k**) 1200 μm/s and (**l**) 200 μm/s. The solder bead is outlined in red and the trap created by the light pattern is outlined in white. D is the centre-to-centre distance between the solder bead and the light pattern.

Once the speed has been determined, DEP force that exert on solder bead can be calculated by the Stokes' law with Faxen's correction (**Eq.2.6-2.8**). We have achieved a maximum speed of 2800 μm/s for a 45 μm solder bead trapped by light patterns with 60 μm and 100 μm diameters, corresponding to a DEP force of 3.27 nN. Compared with optical tweezers which exert forces

at pN level[14], a DEP force of 3.27 nN is quite large. Dependence of DEP force on the centre-to-centre distance between the solder bead and the light pattern is shown in **Fig.3.15**, which quantitatively confirms solder bead will experience a larger DEP force at the edge of the trap. The error bars come from the uncertainty in the measurement of the centre-to-centre distance.

The full range of data used to calculate centre-to-centre distance, DEP force and error bars of the 45 μm solder beads by different diameter light patterns at different speed is shown in **Appendix A.2**.

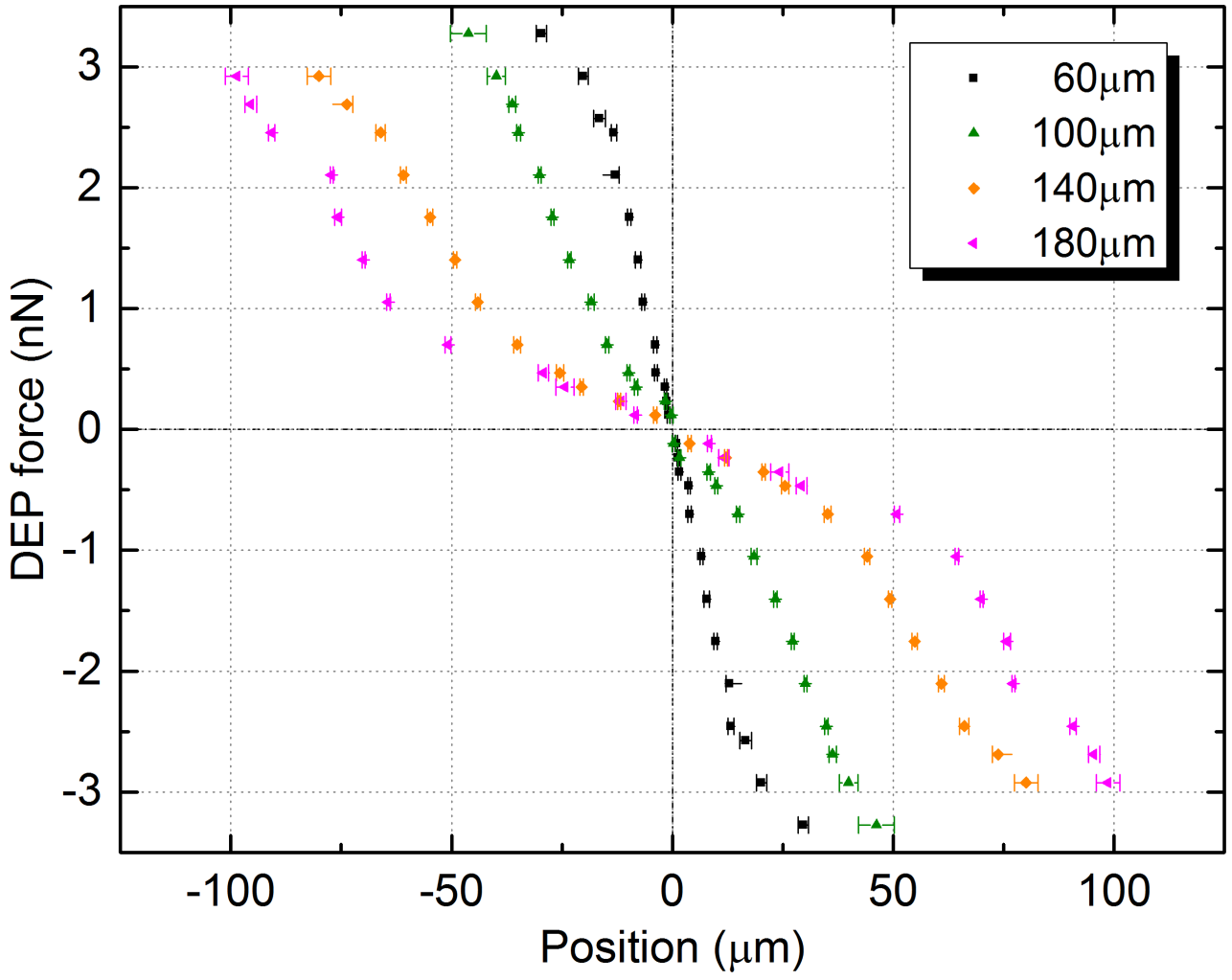

Figure 3.15: Trap profiles of a 45 μm solder bead created by 60 μm, 100 μm, 140 μm and 180 μm diameter light patterns.

3.5 Creating Electrical Connection

Shuailong Zhang et al. succeed in using OET to build a conducting path with sliver nanowires between two isolated metal electrodes and achieved a resistance around 700 Ω[47]. It is a strong proof that OET can be used to create electrical connection but 700 Ω is too high to act as an ideal conducting path. Based on the previous works, our experiment investigated different types of conducting materials including solder and carbon nanotubes (CNTs) in order to have better electrical connection with a lower resistance. Solder is a type of fusible metal alloy that is widely used in making electrical connections among metal workpieces. Previous experimental data confirms that solder beads can experience a strong DEP force in OET device, which makes them easily to be manipulated. Furthermore, a permanent solder bond with a low resistance is formed by a melt process. CNTs are an allotrope of carbon with a cylindrical nanostructure, which have extraordinary thermal, mechanical and electrical properties. The goal of assembly is to construct a conducting path between two isolated metal electrodes on the bottom electrodes. The two metal (gold) electrodes is deposited on the top of the photosensitive layer and have the gap ranging from 50 μm to 400 μm.

3.5.1 Assembly

During the assembly of solder beads, there is a phenomenon that solder bead is strongly attached to metal electrode and can no longer be manipulated by light patterns. The theory of light induced dielectrophoresis (LIDEP) can be used to explain this phenomenon. Light can increase the conductivity in a specific area on the photosensitive layer therefore forms the LIDEP. However, the conductivity of gold (10^7 S/m[86]) is much higher than the conductivity of a-Si:H (10^{-6} S/m for dark conductivity, 10^{-5} S/m for illuminated conductivity[25]) so that solder bead will experience a much larger DEP force at metal electrode than a-Si:H. This phenomenon is helpful to assemble the first solder bead on each metal electrode (**Fig.3.16**(**a**)). It should be noted that the first two solder beads should have a relatively large diameter (around 45 μm) so that the following solder beads will not easily be attached to metal electrodes again.

After the assembly of the first two solder beads, the following solder beads can be precisely manipulated and positioned to build a straight line. Parallel manipulation is used to prevent the interaction between previous assembled solder beads and light patterns which used to manipulate following solder beads. To do so, additional light patterns are applied to trap the previous assembled solder beads (**Fig.3.16**(**b**)) and at the same time the following solder beads can be manipulated to fill in the gap (**Fig.3.16**(**c**)). After we turn off the data projector that used to produce the light, the assembly process is finished (**Fig.3.16**(**d**)). It should be carefully examined that there are no gaps among solder beads so that a good solder bond can form after a melt process.

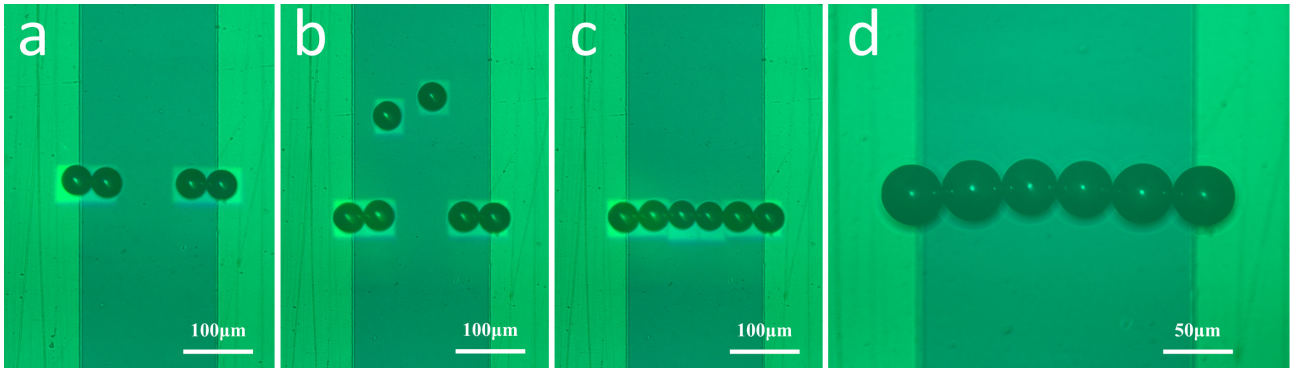

Figure 3.16: Optical microscope images of (**a**) additional light patterns used to trap the previous assembled solder beads. (**b**)-(**c**) Precisely parallel manipulating solder beads to build a straight line. (**d**) The assembly process is completed after the we turn off the data projector (light source).

3.5.2 Freeze-drying

Since the assembly process is surrounded by liquid solution, these surrounding liquid has to be remove before the melt process. Our first try at removing the surrounding liquid is natural evaporation which is used in assembling silver nanowires conducting path[47]. The advantage of natural evaporation is no need for any additional process. However, there is a fatal flaw in this method for assembling solder beads. A slow water wave is formed during evaporating, which swept away these micro-objects and destroy the assembled conducting path (**Fig.3.17**). Thus, removing surrounding liquid without destroying the assembled solder conducting path remains a problem.

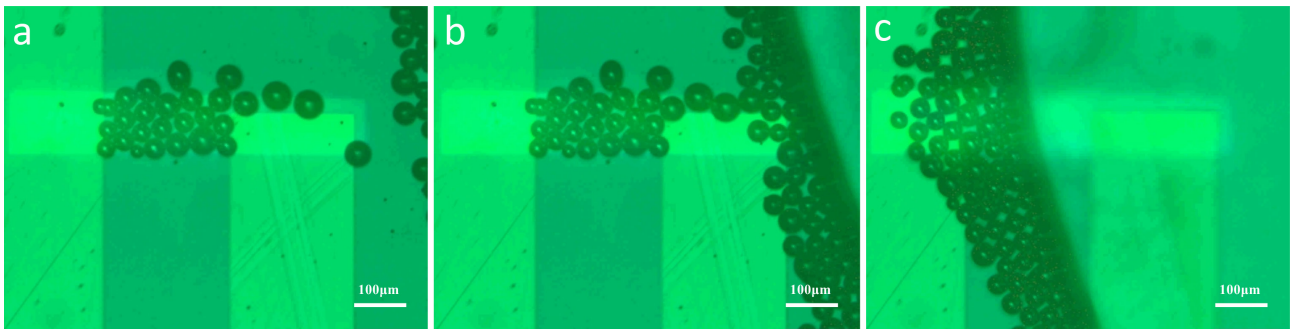

Figure 3.17: Natural evaporation formed water wave swept away the assembled solder beads.

Shuailong Zhang first proposed the use of freeze-drying process in OET to remove the surrounding liquid. This method solves the problem well but needs additionally equipment. Therefore, a series of experiments are set up to promote the idea to a feasible method so that these micro-objects can adhere to the bottom surface at the same place.

Here, we develop a two-stage freezing method that consists of a first refrigeration stage (-12 °C) and a second deep frozen (-80 °C) stage. The first refrigeration stage needs a thermoelectric cooler which utilizes Peltier effect to create heat flux then cool down the OET device. The thermoelectric cooler is placed between the OET device and the motorised stage (ProScan II H101A, **Fig.3.1**(**c**)). A laboratory DC power supply (IPS 2303D, **Fig.3.1**(**g**)) is used to control the temperature of the thermoelectric cooler. The first refrigeration stage serves two purposes: it stops the natural evaporation after assembly and it prevents the move of assembled conducting path when we transfer the sample to a deep freezer. It should be noted that a too fast freezing may break the conducting path. **Fig.3.18** gives an example of this negative effect. Three solder beads have been manipulated to fill in a 50 μm gap (**Fig.3.18**(**a**)). The left end of the assembled line moves down during the freezing process (**Fig.3.18**(**b**)) in which the thermoelectric cooler is directly set to the minimum temperature (-12 °C). After sublimation (**Fig.3.18**(**c**)), the too fast freezing effect can be seen clearly that the whole assembled line moves rightward and the left end of the line can no longer contact the metal electrode. It should be noted that the rightward movement actually happened in the freezing process rather than sublimation because we have verified that the sublimation cannot influence the previous assembled position in **Fig.3.20**(**d**)-(**f**) and **Fig.3.24**(**b**)-(**c**). In addition, the assembled line can no longer be distinguished by optical microscope when the liquid chamber is fully frozen.

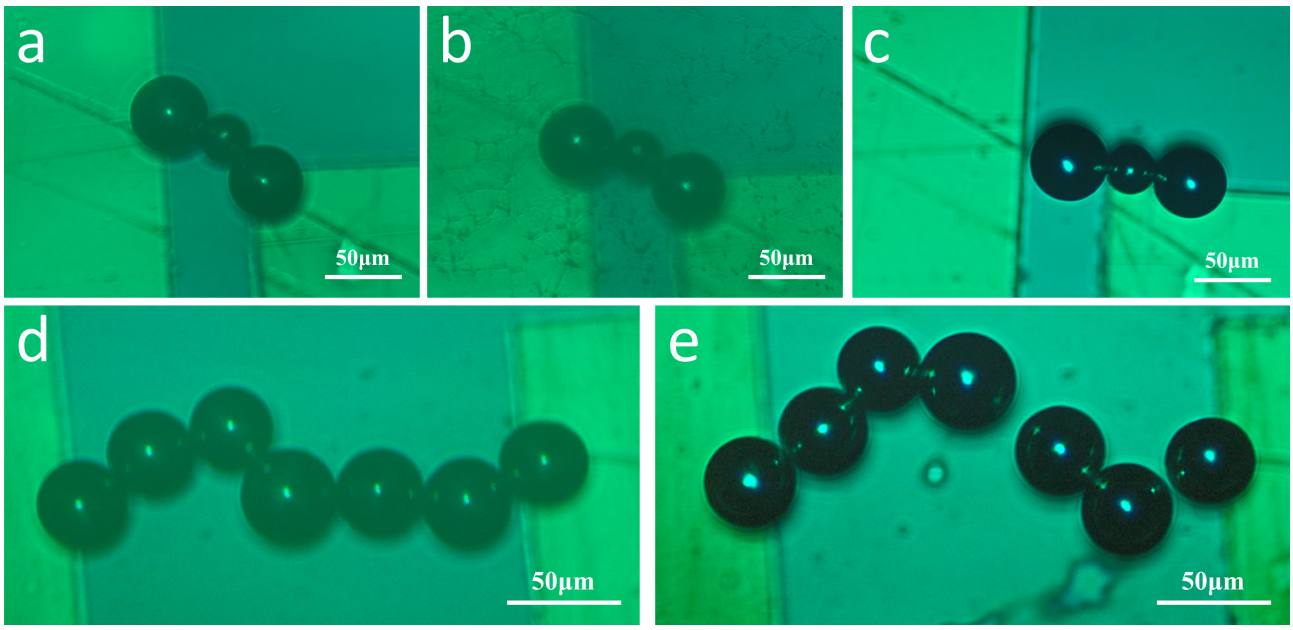

Figure 3.18: Optical microscope images of the assembled conducting path (**a**),(**d**) before freezing, (**b**) during freezing and (**c**),(**e**) after sublimation under a too fast freeze situation.

We further proposed the quantitative measurements of the too fast freeze effect, which based on the centre-to-centre distance of the same solder bead before (**Fig.3.19**(**a**)-(**b**)) and after (**Fig.3.19**(**c**)-(**d**)) a freeze-drying process under a too fast freeze situation. Results show that this negative effect will lead to an average moving distance of 26 μm for an individual solder bead which means this effect cannot be ignored comparing with its own size (25 μm to 45 μm).

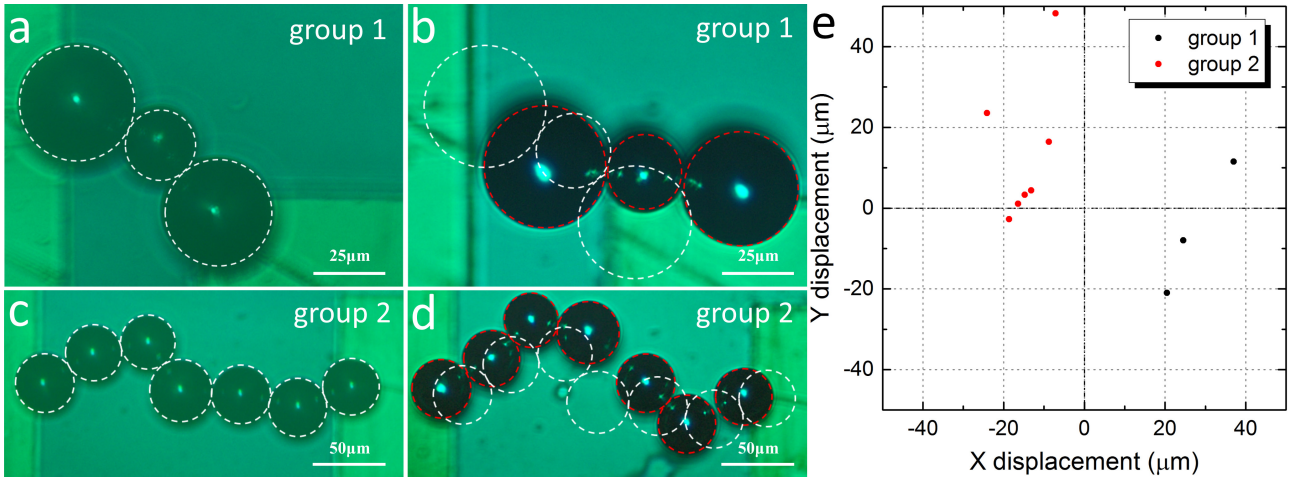

Figure 3.19: (**a**)-(**d**) The quantitative measurements of the too fast freeze effect in which the solder beads are outlined in white (before freeze) and red (after sublimation). (**e**) The distribution of moving distance in X-axis direction and Y-axis direction.

The full range of data used to calculate moving distance before and after a freeze-drying process under a too fast freeze situation is shown in **Appendix D**.

Since the too fast freeze effect can cause a large moving distance, we optimised the first refrigeration stage and developed a step-by-step freezing process to avoid this negative effect. The key point in the step-by-step freezing process is to slow down the freezing rates so that there is no sudden freezing. In our experiment, we controlling the freezing rates by controlling the input current of the thermoelectric cooler at 1.5 A in 1 min, 2 A in 2 min, 2.5 A in 3 min and 3 A in 5 min. It should be noted that the input power of the fan at the thermoelectric cooler should be carefully determined, otherwise the shake of thermoelectric cooler caused by high fan speed may break the assembled line.

Once the first refrigeration stage is done, the whole OET device is immediately transferred to a deep freezer (-80 °C) to carry out the second deep frozen stage (1 hour). After that, a freeze drying system (PowerDry LL3000, **Fig.3.1(l)**) is used to sublimate the frozen liquid.

A successful freeze-drying process is shown in **Fig.3.20**. It can be seen clearly that the assembled line remains its structure without any movement after an optimised freeze-drying process.

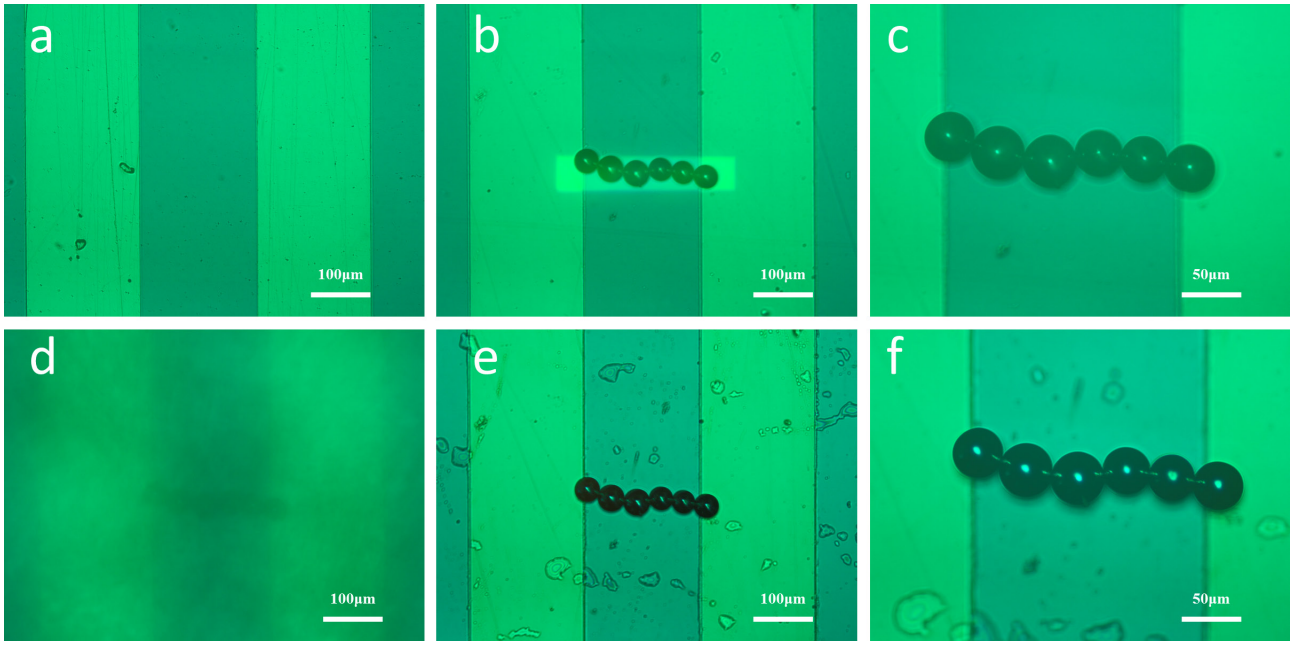

Figure 3.20: Optical microscope images of (**a**) two isolated metal electrodes with a 200 μm gap before the assembly of solder beads. (**b**)-(**c**) An assembled line with solder beads. (**d**) The first refrigeration stage. (**e**)-(**f**) The assembled line after freeze-drying.

3.5.3 Melt

After the freeze-drying process, the bottom photosensitive electrode with assembled solder beads is put onto a hot plate (Cole-Parmer StableTemp, **Fig.3.1**(**j**)) for a melt process. We set up a series of temperature to investigate the step-by-step melt process of solder beads (**Table 3.2**). It should be noted that the melting point of solder bead we used is 179 °C.

Table 3.2: The step-by-step melt process.

temperature (°C)	time (min)	result
185	1	**Fig.3.21**(**a**) & **Fig.3.24**(**d**)
185	3	**Fig.3.21**(**b**) & **Fig.3.24**(**e**)
250	5	**Fig.3.21**(**c**) & **Fig.3.24**(**f**)

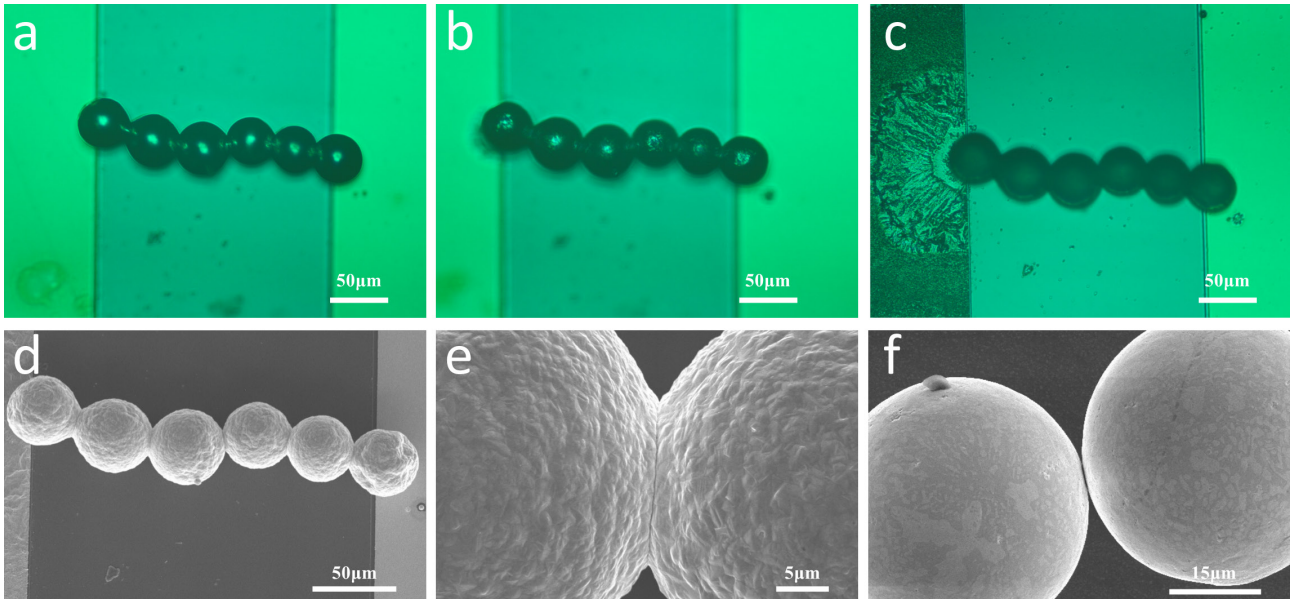

Figure 3.21: Optical microscope images of the assembled line during a step-by-step melt process at (**a**) 185 °C in 1 min, (**b**) 185 °C in 3 min and (**c**) 250 °C in 5 min. SEM images of the assembled line (**d**)-(**e**) after and (**f**) before a step-by-step melt process.

Fig.3.21 shows the shape changes during the step-by-step melt process. The assembled solder line is the same as **Fig.3.20**. Under a temperature of 185 °C, the spherical surface of solder beads becomes rough and solder bond is formed among solder beads (**Fig.3.21**(**a**)-(**b**)). After a high temperature melting (250 °C, **Fig.3.21**(**c**)), the shape of solder beads changes from spherical to irregular and the left end of solder bead melted into a large area on metal electrode (**Fig.3.21**(**c**)). The solder bond between solder beads can be seen clearly in SEM images **Fig.3.21**(**d**)-(**e**). **Fig.3.21**(**f**) shows two assembled solder beads before melt without

the formation of solder bond.

Since the thermal conductivity of gold (314 $Wm^{-1}K^{-1}$[87]) is much higher than the thermal conductivity of a-Si:H (below 2 $Wm^{-1}K^{-1}$ at thin film structure[88]), the solder beads melt faster on metal electrode than photosensitive layer. To investigate the melt situation, a series of SEM images for discrete solder beads on different surface are taken (**Fig.3.22**).

The surface morphology of a discrete melted solder bead on metal electrode is shown in **Fig.3.22**(**a**) in which the spherical surface of solder bead has changed to an irregular shape. Compared with **Fig.3.21**(**e**), more solder melted on metal electrode than photosensitive layer. **Fig.3.22**(**b**) gives a direct comparison of melt situation showing a discrete solder bead melted at the junction between photosensitive layer (left) and metal electrode (right). It can be seen that a large proportion of solder melted on the metal electrode and expanded to a large solder layer. The boundary of melted solder on metal electrode is shown in **Fig.3.22**(**c**).

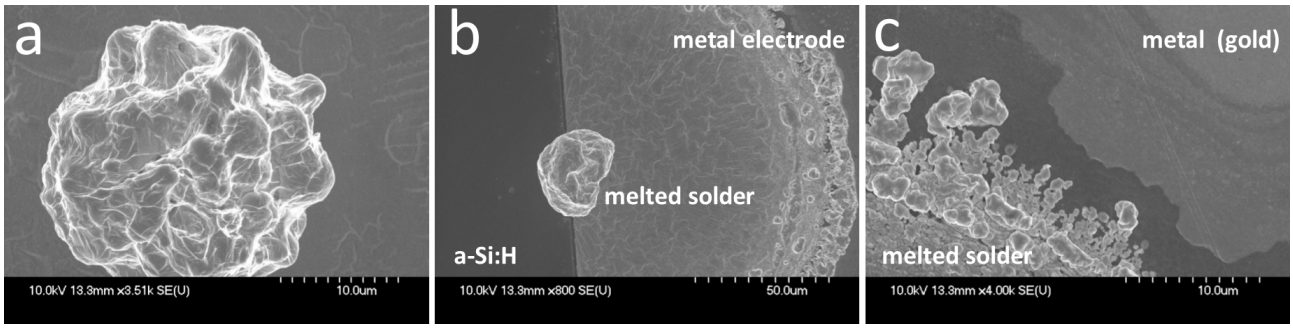

Figure 3.22: SEM images of (**a**) a melted solder bead on metal electrode, (**b**) a melted solder bead at the junction between a-Si:H and metal electrode and (**c**) the boundary of melted solder on metal electrode.

The melt speed difference due to thermal conductivity gives us a sign (the expanded solder on metal) to judge whether the electrical connection between metal and solder is formed or not.

3.5.4 Assembly of Carbon Nanotubes (CNTs)

CNTs were dispersed into a liquid solution (0.05%, TWEEN 20) done by a mixer so that micron level CNTs cluster are formed. **Fig.3.23** demonstrates the use of OET in manipulating CNTs into a 150 μm gap between two isolated metal electrodes.

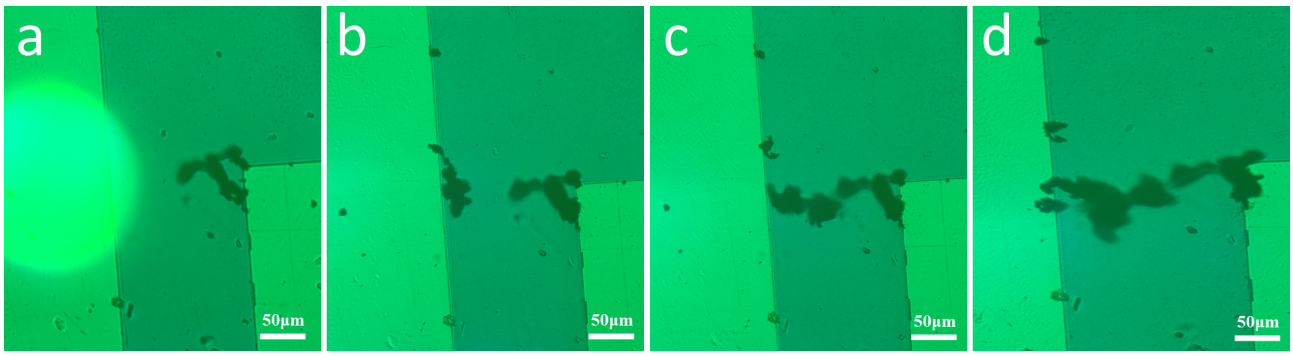

Figure 3.23: Optical microscope images of assembling CNTs into a gap between two isolated metal electrodes.

After assembly, the surrounding liquid is removed by natural evaporation which is suitable for silver nanowires[47]. However, the assembled structure is completely destroyed by natural evaporation formed water wave. Density difference can be used to explain this phenomenon. The density of silver nanowires they used is 0.785 g/mL while the bulk density of CNTs we used is 0.091 g/mL. Assemble silver nanowires conducting path will attach to the substrate and experience a strong Van der Waals force so that the water wave cannot destroy its structure. Assembled CNTs cluster however, will float in the liquid solution so that the water wave can easily destroy its structure.

3.5.5 Current-Voltage Characteristic

A whole assemble-freeze-drying-melt process is shown in **Fig.3.24**(**a**)-(**f**). Before the assembly of the conducting path, there is no flow of current through the two isolated metal electrodes. After the formation of a permanent solder conducting path (**Fig.3.24**(**f**)), the current-voltage (IV) characteristic of this conducting path has been measured by a probe station (CascadeMicrotech MPS150, **Fig.3.1**(**m**)). Two probes are placed on two isolated metal electrodes, separately. Experimental data generated by semiconductor device analyzer (Keysight B1500A, **Fig.3.1**(**k**)) demonstrates a linear IV curve (**Fig.3.24**(**g**)) achieving a low resistance of 11.6 Ω. This proves that OET can be used to create a good electrical connection, which holds great potential for micron level circuits construction.

The full range of data used to calculate the resistance is shown in **Appendix C**.

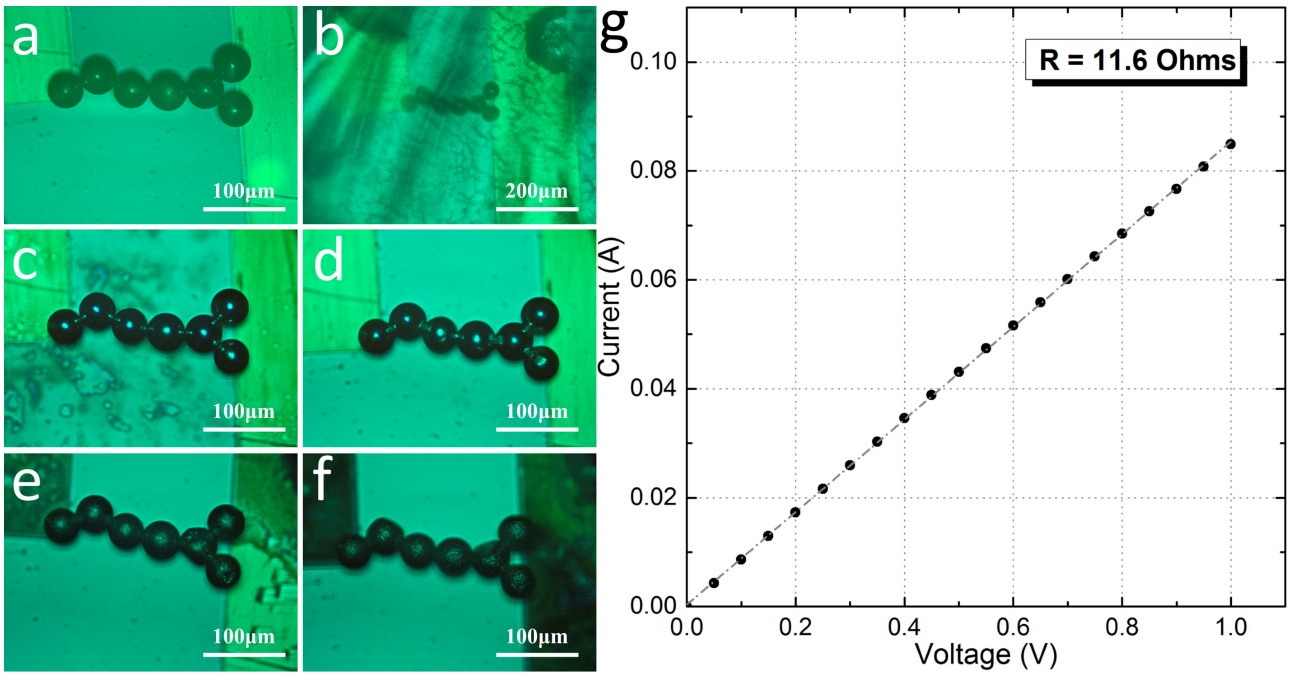

Figure 3.24: (**a**)-(**f**) Optical microscope images of a whole assemble-freeze-drying-melt process for solder beads. (**a**) An assembled line with solder beads. (**b**) The first refrigeration stage for the assembled line. (**c**) The assembled line after freeze-drying. The assembled line after a step-by-step melt process at (**d**) 185 °C in 1 min, (**e**) 185 °C in 3 min and (**f**) 250 °C in 5 min. (**g**) I-V characteristics of the two isolated metal electrodes after a whole assemble-freeze-drying-melt process for solder beads. A conducting path is formed.

3.6 Moving Electronic and Optoelectronic Components

The conducting path we created with OET proves the capacity of OET to create a good electrical connection. Previous published works on moving micro-resistor[48] and semiconductor laser[49] indicate the capacity of OET for manipulating discrete electronic and optoelectronic components. The next step is to assemble electronic and optoelectronic components into circuits. We divided it into a two-stage experiment. First, we will try to move electronic and optoelectronic components to a specific position with OET. Second, assembling conductive micro-objects such as solder beads and CNTs with OET to contact these components and achieve the electrical connection.

These micro-LEDs have the size of size of 100 μm $\times$ 100 μm which is suitable for OET manipulation but we have not succeeded in moving a whole micro-LED yet. However, the fragments of these micro-LEDs experienced a strong positive DEP force in OET device so that we demonstrated the manipulation of these fragments in **Fig.3.25**(**a**).

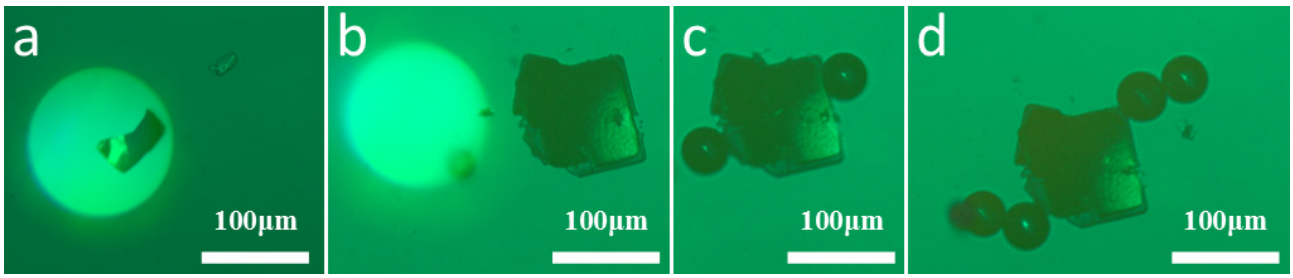

Figure 3.25: Optical microscope images of (**a**) moving a fragment of micro-LED and manipulating (**c**) two and (**d**) four solder beads to contact to (**b**) a discrete GaN micro-LED.

The assembly of conductive micro-objects to contact to micro-LED is our next step. **Fig.3.25**(**b**)-(**d**) demonstrate the procedure of assembling solder beads to contact to a discrete micro-LED at the correct gold tracks position.

Chapter 4

Conclusion

4.1 Summary of Thesis Achievements

We demonstrated the use of OET to manipulate micro-objects including silver-coated PMMA microspheres, solder beads, carbon nanotubes (CNTs) and part of GaN micro-LEDs.

We investigated the prerequisites of building functional circuits with OET, which are electrical connection and components manipulation. We proposed a feasible method for creating electrical connection including assembly, freeze-drying and step-by-step melt. Parallel manipulation technique is used in assembly. Quantitative analysis of the too fast freeze effect shows an average moving distance of 26 μm for an individual solder bead. Natural evaporation for assembled solder conducting line and melt situation on different substrate have also been examined.

Current-voltage characteristic shows a low resistance of 11.6 Ω, which proves the capacity of OET in creating good electrical connection. Accuracy and speed of assembly have been investigated in a series of experiments as well. The distribution after random movement demonstrates a qualitative relationship between light pattern diameter and accuracy, in which the distribution of solder beads become more discrete with the increase of the light pattern diameter. Furthermore, we proposed a quantitative definition of accuracy and found that the positioning deviation of the solder beads increases linearly with the increase of the light pattern diameter.

The investigation into accuracy indicates a way to choose an appropriate light pattern size in assembly. The highest accuracy we achieved is 0.8 ± 0.1 μm with 60 μm diameter light pattern for 45 μm solder beads. We have achieved a maximum speed of 2800 μm/s for a 45 μm solder bead trapped by light patterns with 60 μm and 100 μm diameters at 25 V_{pp}, 15 kHz, corresponding to a DEP force of 3.27 nN which is much larger than optical tweezers (pN level). We demonstrate the manipulation of solder beads to contact to micro-LED, which indicates the potential application in building functional circuits with OET.

Two publications can be found at Ref.[89],[90].

4.2 Future Works

Future works involve building conducting path with other materials, creating functional circuits with OET, computer vision based manipulation and 3D printing based encapsulation.

More specifically, CNTs can be dispersed into mesoscopic level for assembly, solder beads can be assembled into different gaps, the contact between solder beads and micro-LED can be melted to see if there is electrical connection, the integration of Maxwell stress tensor based simulation can be used to support the experiment, computer vision can be used to accurately assemble conducting path and 3D printing can be used to encapsulate the assembled conducting path.

References

[1] Arthur Ashkin, JM Dziedzic, JE Bjorkholm, and Steven Chu. Observation of a single-beam gradient force optical trap for dielectric particles. *Optics letters*, 11(5):288–290, 1986.

[2] Arthur Ashkin. History of optical trapping and manipulation of small-neutral particle, atoms, and molecules. *IEEE Journal of Selected Topics in Quantum Electronics*, 6(6):841–856, 2000.

[3] Arthur Ashkin. Acceleration and trapping of particles by radiation pressure. *Physical review letters*, 24(4):156, 1970.

[4] Arthur Ashkin, JM Dziedzic, and T Yamane. Optical trapping and manipulation of single cells using infrared laser beams. *Nature*, 330(6150):769–771, 1987.

[5] Karel Svoboda and Steven M Block. Optical trapping of metallic rayleigh particles. *Optics letters*, 19(13):930–932, 1994.

[6] Pu Chun Ke and Min Gu. Characterization of trapping force on metallic mie particles. *Applied optics*, 38(1):160–167, 1999.

[7] Lucien P Ghislain, Neil A Switz, and Watt W Webb. Measurement of small forces using an optical trap. *Review of Scientific Instruments*, 65(9):2762–2768, 1994.

[8] Alexander Rohrbach and Ernst HK Stelzer. Trapping forces, force constants, and potential depths for dielectric spheres in the presence of spherical aberrations. *Applied optics*, 41(13):2494–2507, 2002.

[9] Rustem I Litvinov, Henry Shuman, Joel S Bennett, and John W Weisel. Binding strength and activation state of single fibrinogen-integrin pairs on living cells. *Proceedings of the National Academy of Sciences*, 99(11):7426–7431, 2002.

[10] Eric R Dufresne and David G Grier. Optical tweezer arrays and optical substrates created with diffractive optics. *Review of scientific instruments*, 69(5):1974–1977, 1998.

[11] Eric R Dufresne, Gabriel C Spalding, Matthew T Dearing, Steven A Sheets, and David G Grier. Computer-generated holographic optical tweezer arrays. *Review of Scientific Instruments*, 72(3):1810–1816, 2001.

[12] Ming C Wu. Optoelectronic tweezers. *Nature Photonics*, 5(6):322–324, 2011.

[13] MICHAEL W Berns. A possible two-photon effect in vitro using a focused laser beam. *Biophysical journal*, 16(8):973, 1976.

[14] David G Grier. A revolution in optical manipulation. *Nature*, 424(6950):810–816, 2003.

[15] Herbert A Pohl and Ira Hawk. Separation of living and dead cells by dielectrophoresis. *Science*, 152(3722):647–649, 1966.

[16] Peter RC Gascoyne, Xiao-Bo Wang, Ying Huang, and Frederick F Becker. Dielectrophoretic separation of cancer cells from blood. *IEEE transactions on industry applications*, 33(3):670–678, 1997.

[17] Dino Di Carlo, Jon F Edd, Daniel Irimia, Ronald G Tompkins, and Mehmet Toner. Equilibrium separation and filtration of particles using differential inertial focusing. *Analytical chemistry*, 80(6):2204–2211, 2008.

[18] Pei-Yu Chiou. *Massively parallel optical manipulation of single cells, micro-and nanoparticles on optoelectronic devices*. PhD thesis, UNIVERSITY OF CALIFORNIA AT BERKELEY, 2005.

[19] Nicoló Manaresi, Aldo Romani, Gianni Medoro, Luigi Altomare, Andrea Leonardi, Marco Tartagni, and Roberto Guerrieri. A cmos chip for individual cell manipulation and detection. *IEEE Journal of Solid-State Circuits*, 38(12):2297–2305, 2003.

[20] Pei Yu Chiou, Zehao Chang, and Ming C Wu. A novel optoelectronic tweezer using light induced dielectrophoresis. In *Optical MEMS, 2003 IEEE/LEOS International Conference on*, pages 8–9. IEEE, 2003.

[21] Pei Yu Chiou, Aaron T Ohta, and Ming C Wu. Massively parallel manipulation of single cells and microparticles using optical images. *Nature*, 436(7049):370–372, 2005.

[22] Peter Gascoyne, Chulabhorn Mahidol, Mathuros Ruchirawat, Jutamaad Satayavivad, Piyajit Watcharasit, and Frederick F Becker. Microsample preparation by dielectrophoresis: isolation of malaria. *Lab on a Chip*, 2(2):70–75, 2002.

[23] Frederick F Becker, Xiao-Bo Wang, Ying Huang, Ronald Pethig, Jody Vykoukal, and PR Gascoyne. Separation of human breast cancer cells from blood by differential dielectric affinity. *Proceedings of the National Academy of Sciences*, 92(3):860–864, 1995.

[24] Jun Yang, Ying Huang, Xiao-Bo Wang, Frederick F Becker, and Peter RC Gascoyne. Differential analysis of human leukocytes by dielectrophoretic field-flow-fractionation. *Biophysical Journal*, 78(5):2680–2689, 2000.

[25] SL Neale, M Mazilu, JIB Wilson, K Dholakia, and TF Krauss. The resolution of optical traps created by light induced dielectrophoresis (lidep). *Optics express*, 15(20):12619–12626, 2007.

[26] Pei-Yu Chiou, Aaron T Ohta, and Ming C Wu. Toward all optical lab-on-a-chip system: optical manipulation of both microfluid and microscopic particles. In *Optical Science and Technology, the SPIE 49th Annual Meeting*, pages 73–81. International Society for Optics and Photonics, 2004.

[27] Aaron T Ohta, Pei-Yu Chiou, Huan L Phan, Steven W Sherwood, Joon M Yang, Aldrich NK Lau, Hsan-Yin Hsu, Arash Jamshidi, and Ming C Wu. Optically controlled cell discrimination and trapping using optoelectronic tweezers. *IEEE Journal of Selected Topics in Quantum Electronics*, 13(2):235–243, 2007.

[28] Aaron T Ohta, Steven L Neale, Hsan-Yin Hsu, Justin K Valley, and Ming C Wu. Parallel assembly of nanowires using lateral-field optoelectronic tweezers. In *2008 IEEE/LEOS International Conference on Optical MEMS and Nanopotonics*, 2008.

[29] Hyundoo Hwang, Youngjae Oh, Jae-Jun Kim, Wonjae Choi, Je-Kyun Park, Se-Hwan Kim, and Jin Jang. Reduction of nonspecific surface-particle interactions in optoelectronic tweezers. *Applied Physics Letters*, 92(2):024108, 2008.

[30] Arash Jamshidi, Peter J Pauzauskie, P James Schuck, Aaron T Ohta, Pei-Yu Chiou, Jeffrey Chou, Peidong Yang, and Ming C Wu. Dynamic manipulation and separation of individual semiconducting and metallic nanowires. *Nature Photonics*, 2(2):86–89, 2008.

[31] John C Crocker and David G Grier. Methods of digital video microscopy for colloidal studies. *Journal of colloid and interface science*, 179(1):298–310, 1996.

[32] Arash Jamshidi. *Optoelectronic Manipulation, assembly, and patterning of nanoparticles.* PhD thesis, University of California, Berkeley, 2009.

[33] John A Rogers. Optoelectronic tweezers: Organizing nanowires. *Nature Photonics*, 2(2):69–70, 2008.

[34] Antonio Ramos, Hywel Morgan, Nicolas G Green, and Antonio Castellanos. Ac electric-field-induced fluid flow in microelectrodes. *Journal of colloid and interface science*, 217(2):420–422, 1999.

[35] Pei-Yu Chiou, Aaron T Ohta, Arash Jamshidi, Hsin-Yi Hsu, and Ming C Wu. Light-actuated ac electroosmosis for nanoparticle manipulation. *Journal of Microelectromechanical Systems*, 17(3):525–531, 2008.

[36] Antonio Castellanos, Antonio Ramos, Antonio Gonzalez, Nicolas G Green, and Hywel Morgan. Electrohydrodynamics and dielectrophoresis in microsystems: scaling laws. *Journal of Physics D: Applied Physics*, 36(20):2584, 2003.

[37] Arash Jamshidi, Steven L Neale, Kyoungsik Yu, Peter J Pauzauskie, Peter James Schuck, Justin K Valley, Hsan-Yin Hsu, Aaron T Ohta, and Ming C Wu. Nanopen: dynamic,

low-power, and light-actuated patterning of nanoparticles. *Nano letters*, 9(8):2921–2925, 2009.

[38] Arash Jamshidi, Hsan-Yin Hsu, Justin K Valley, Aaron T Ohta, Steven Neale, and Ming C Wu. Metallic nanoparticle manipulation using optoelectronic tweezers. In *Micro Electro Mechanical Systems, 2009. MEMS 2009. IEEE 22nd International Conference on*, pages 579–582. IEEE, 2009.

[39] Yeonee Seol, Amanda E Carpenter, and Thomas T Perkins. Gold nanoparticles: enhanced optical trapping and sensitivity coupled with significant heating. *Optics letters*, 31(16):2429–2431, 2006.

[40] Aaron T Ohta, Arash Jamshidi, Justin K Valley, Hsan-Yin Hsu, and Ming C Wu. Optically actuated thermocapillary movement of gas bubbles on an absorbing substrate. *Applied physics letters*, 91(7):074103, 2007.

[41] Piotr Garstecki, Michael J Fuerstman, Michael A Fischbach, Samuel K Sia, and George M Whitesides. Mixing with bubbles: a practical technology for use with portable microfluidic devices. *Lab on a Chip*, 6(2):207–212, 2006.

[42] Susan Z Hua, Frederick Sachs, David X Yang, and Harsh Deep Chopra. Microfluidic actuation using electrochemically generated bubbles. *Analytical chemistry*, 74(24):6392–6396, 2002.

[43] Thomas K Jun et al. Valveless pumping using traversing vapor bubbles in microchannels. *Journal of Applied Physics*, 83(11):5658–5664, 1998.

[44] Tomomi Sakata, Hiroyoshi Togo, Mitsuhiro Makihara, Fusao Shimokawa, and Kazumasa Kaneko. Improvement of switching time in a thermocapillarity optical switch. *Journal of lightwave technology*, 19(7):1023–1027, 2001.

[45] Steven L Neale, Aaron T Ohta, Hsan-Yin Hsu, Justin K Valley, Arash Jamshidi, and Ming C Wu. Trap profiles of projector based optoelectronic tweezers (oet) with hela cells. *Optics express*, 17(7):5231–5239, 2009.

[46] Steven L Neale, Nimesh Mody, Colin Selman, and Jonathan M Cooper. Optoelectronic tweezers for the measurement of the relative stiffness of erythrocytes. In *SPIE NanoScience+ Engineering*, pages 845827–845827. International Society for Optics and Photonics, 2012.

[47] Shuailong Zhang, Jonathan M Cooper, and Steve L Neale. Assembling silver nanowires using optoelectronic tweezers. In *SPIE OPTO*, pages 97590S–97590S. International Society for Optics and Photonics, 2016.

[48] Shuailong Zhang, Joan Juvert, Jonathan Cooper, and Steven Neale. Assembling and manipulating metallic beads using optoelectronic tweezers. 2016.

[49] Joan Juvert, Shuailong Zhang, Iain Eddie, Colin J Mitchell, Graham T Reed, James S Wilkinson, Anthony Kelly, and Steven L Neale. Micromanipulation of inp lasers with optoelectronic tweezers for integration on a photonic platform. *Optics Express*, 24(16):18163–18175, 2016.

[50] Aaron T Ohta, Arash Jamshidi, Hsan-Yin Hsu, Justin K Valley, Ming C Wu, Pei-Yu Chiou, and Steven L Neale. *Optoelectronic Tweezers for the Manipulation of Cells, Microparticles, and Nanoparticles*. INTECH Open Access Publisher, 2010.

[51] Herbert Ackland Pohl. Some effects of nonuniform fields on dielectrics. *Journal of Applied Physics*, 29(8):1182–1188, 1958.

[52] Herbert Ackland Pohl and HA Pohl. *Dielectrophoresis: the behavior of neutral matter in nonuniform electric fields*, volume 80. Cambridge university press Cambridge, 1978.

[53] TB Jones. Electromechanics of particles. 1995. *Cambridge, Cambridge*.

[54] Justin K Valley, Arash Jamshidi, Aaron T Ohta, Hsan-Yin Hsu, and Ming C Wu. Operational regimes and physics present in optoelectronic tweezers. *Journal of Microelectromechanical Systems*, 17(2):342–350, 2008.

[55] H Morgan and NG Green. Ac electrokinetics: colloids and nanoparticles. 2003. *Hertfordshire, England: Research Studies Press LTD*, 324.

[56] Karel Svoboda and Steven M Block. Biological applications of optical forces. *Annual review of biophysics and biomolecular structure*, 23(1):247–285, 1994.

[57] Richard BM Schasfoort, Stefan Schlautmann, Jan Hendrikse, and Albert van den Berg. Field-effect flow control for microfabricated fluidic networks. *Science*, 286(5441):942–945, 1999.

[58] Ping Wang, Zilin Chen, and Hsueh-Chia Chang. A new electro-osmotic pump based on silica monoliths. *Sensors and Actuators B: Chemical*, 113(1):500–509, 2006.

[59] J Lyklema. Fundamentals of colloid and interface science. *Solid-Liqiud Interfaces*, 1991.

[60] Hirofumi Daiguji, Peidong Yang, and Arun Majumdar. Ion transport in nanofluidic channels. *Nano Letters*, 4(1):137–142, 2004.

[61] Nicolas G Green, Antonio Ramos, Antonio González, Hywel Morgan, and Antonio Castellanos. Fluid flow induced by nonuniform ac electric fields in electrolytes on microelectrodes. i. experimental measurements. *Physical review E*, 61(4):4011, 2000.

[62] John Paul Urbanski, Todd Thorsen, Jeremy A Levitan, and Martin Z Bazant. Fast ac electro-osmotic micropumps with nonplanar electrodes. *Applied Physics Letters*, 89(14):143508, 2006.

[63] RC Hayward, DA Saville, and IA Aksay. Electrophoretic assembly of colloidal crystals with optically tunable micropatterns. *Nature*, 404(6773):56–59, 2000.

[64] Antonio Ramos, Hywel Morgan, Nicolas G Green, and A Castellanos. Ac electrokinetics: a review of forces in microelectrode structures. *Journal of Physics D: Applied Physics*, 31(18):2338, 1998.

[65] Albert Einstein. *Investigations on the Theory of the Brownian Movement*. Courier Corporation, 1956.

[66] Aaron Takami Ohta, Pei-Yu Chiou, Tae H Han, James C Liao, Urvashi Bhardwaj, Edward RB McCabe, Fuqu Yu, Ren Sun, and Ming C Wu. Dynamic cell and microparticle

control via optoelectronic tweezers. *Journal of Microelectromechanical Systems*, 16(3):491–499, 2007.

[67] Wei Wang, Yen-Heng Lin, Ruei-Syuan Guan, Ten-Chin Wen, Tzung-Fang Guo, and Gwo-Bin Lee. Bulk-heterojunction polymers in optically-induced dielectrophoretic devices for the manipulation of microparticles. *Optics express*, 17(20):17603–17613, 2009.

[68] Shih-Mo Yang, Tung-Ming Yu, Hang-Ping Huang, Meng-Yen Ku, Long Hsu, and Cheng-Hsien Liu. Dynamic manipulation and patterning of microparticles and cells by using tiopc-based optoelectronic dielectrophoresis. *Optics letters*, 35(12):1959–1961, 2010.

[69] Yuichi Higuchi, Tatsuya Kusakabe, Tomoki Tanemura, Koji Sugano, Toshiyuki Tsuchiya, and Osamu Tabata. Manipulation system for nano/micro components integration via transportation and self-assembly. In *2008 IEEE 21st International Conference on Micro Electro Mechanical Systems*, 2008.

[70] Olympus UC30 Microscope Digital Cameras. Retrieved from http://www.olympus-ims.com/en/microscope/uc30/

[71] Olympus BX51. Retrieved from http://www.olympus-ims.com/en/microscope/bx51p/

[72] ProScan II H101A stage. Retrieved from http:// www.prior-us.com/Products/Motorized-Stages/h101a.aspx

[73] Dell 1510X Projector. Retrieved from https://www.dell.com/learn/us/en/vn/corp-comm/image-gallery-projectors

[74] ProScan III H31 Automation Controller. Retrieved from http:// www.prior-us.com/Products/Controllers/V31XYZ.aspx

[75] Proscan III PS3J100 Interactive control Centre. Retrieved from http:// www.prior-us.com/Products/Accessories/PS3J100.aspx

[76] IPS 2303D. Retrieved from http://www.iso-techonline.com/product/

[77] TTi TG5011 50MHz function/arbitrary/pulse generator. Retrieved from http://tti-test.com/go/tg5011/index.htm

[78] TTi WA301 Wideband 30V pk-pk amplifier for waveform generation. Retrieved from http://www.ttid.co.uk/waveform-amplifiers/aim-tti/wa301

[79] Cole-Parmer StableTemp Hot Plates. Retrieved from http://www.coleparmer.com/ Product/StableTemp_Ceramic_Hot_Plate_7_x_7_120_VAC/EW-03405-10

[80] Keysight B1500A Semiconductor Device Analyzer. Retrieved from http://www.keysight.com/en/pd-582565-pn-B1500A/semiconductor-device-analyzer

[81] Thermo Scientific Heraeus PowerDry LL3000 Freeze drying systems. Retrieved from https://www.fishersci.co.uk/webfiles/uk/web-docs/UKLS_0737.PDF

[82] CascadeMicrotech MPS150 Manual Probe System. Retrieved from https://www.cascademicrotech.com/products/probe-systems/150mm-wafer

[83] Hitachi S-4700 SEM. Retrieved from http:// www.hitachi-hightech.com/us/product_list/?ld=sms2&md=sms2-1

[84] SUSS MicroTec MA6. Retrieved from http:// www.suss.com/en/products-solutions/products/mask-aligner.html

[85] AJ Trindade, B Guilhabert, EY Xie, R Ferreira, JJD McKendry, D Zhu, N Laurand, E Gu, DJ Wallis, IM Watson, et al. Heterogeneous integration of gallium nitride light-emitting diodes on diamond and silica by transfer printing. *Optics express*, 23(7):9329–9338, 2015.

[86] Raymond A Serway. Principles of physics. fort worth, texas; london: Saunders college pub. Technical report, ISBN 0-03-020457-71998, 1998.

[87] D Young Hugh and Roger A Freedman. *University physics*. Addison-Wesley, 1992.

[88] David G Cahill, My Katiyar, and JR Abelson. Thermal conductivity of a-si:h thin films. *Physical review B*, 50(9):6077, 1994.

[89] Shuailong Zhang, Yongpeng Liu, Joan Juvert, Pengfei Tian, Jean-Claude Navarro, Jonathan M Cooper, and Steven L Neale. Use of optoelectronic tweezers in manufacturingaccurate solder bead positioning. *Applied Physics Letters*, 109(22):221110, 2016.

[90] Shuailong Zhang, Yongpeng Liu, Yang Qian, Weizhen Li, Joan Juvert, Pengfei Tian, Jean-Claude Navarro, Alasdair W Clark, Erdan Gu, Martin D Dawson, Jonathan M Cooper, and Steven L Neale. Manufacturing with light-micro-assembly of opto-electronic microstructures. *Optics Express*, 25(23):28838–28850, 2017.

Appendix A

Full Data of the 45 μm Solder Beads

A.1 Displacements & Accuracy

Table A.1: Displacements & Accuracy.

60μm								
group	light (μm)		bead (μm)		offset (μm)		accuracy (μm)	
	X	Y	X	Y	X	Y	ΔX	ΔY
1	0.0	0.0	-1.7	-0.7	-1.7	-0.7		
2	70.0	-100.0	67.2	-100.3	-2.8	-0.3	1.0	0.3
3	260.0	90.0	259.0	89.0	-1.0	-1.0	1.7	0.7
4	160.0	-130.0	157.2	-129.0	-2.8	1.0	1.7	2.1
5	-10.0	-260.0	-11.7	-260.0	-1.7	0.0	1.0	1.0
6	180.0	90.0	177.9	90.3	-2.1	0.3	0.3	0.3
7	80.0	-120.0	77.9	-119.0	-2.1	1.0	0.0	0.7
8	-280.0	290.0	-280.3	290.3	-0.3	0.3	1.7	0.7
9	150.0	-110.0	150.0	-109.3	0.0	0.7	0.3	0.4
10	-240.0	110.0	-240.7	110.3	-0.7	0.3	0.7	0.3
11	10.0	140.0	9.7	141.0	-0.4	1.0	0.3	0.7
12	-90.0	30.0	-91.7	30.7	-1.7	0.7	1.4	0.3
			average		-1.4	0.3	0.9	0.7

80μm								
group	light (μm)		bead (μm)		offset (μm)		accuracy (μm)	
	X	Y	X	Y	X	Y	ΔX	ΔY
1	0.0	0.0	-1.4	1.7	-1.4	1.7		
2	-230.0	-30.0	-231.7	-27.9	-1.7	2.1	0.3	0.4
3	170.0	-390.0	168.3	-388.6	-1.7	1.4	0.0	0.7
4	-60.0	0.0	-60.4	1.0	-0.4	1.0	1.4	0.4
5	-260.0	330.0	-261.7	332.4	-1.7	2.4	1.4	1.4
6	-130.0	-120.0	-130.7	-117.6	-0.7	2.4	1.0	0.0
7	140.0	-190.0	141.4	-189.7	1.4	0.3	2.1	2.1
8	360.0	320.0	360.0	321.4	0.0	1.4	1.4	1.0
9	340.0	-170.0	339.0	-167.2	-1.0	2.8	1.0	1.4
10	-230.0	340.0	-233.5	341.7	-3.5	1.7	2.4	1.0
11	-280.0	220.0	-280.4	222.4	-0.4	2.4	3.1	0.7
12	140.0	-220.0	138.6	-217.9	-1.4	2.1	1.0	0.4
			average		-1.0	1.8	1.4	0.9

100μm								
group	light (μm)		bead (μm)		offset (μm)		accuracy (μm)	
	X	Y	X	Y	X	Y	ΔX	ΔY
1	0.0	0.0	-2.8	0.0	-2.8	0.0		
2	10.0	70.0	7.9	72.8	-2.1	2.8	0.7	2.8
3	370.0	-350.0	370.4	-349.3	0.4	0.7	2.4	2.1
4	-120.0	420.0	-122.8	417.9	-2.8	-2.1	3.1	2.8
5	40.0	-270.0	36.9	-269.3	-3.1	0.7	0.3	2.8
6	-350.0	-50.0	-353.5	-50.0	-3.5	0.0	0.3	0.7
7	270.0	130.0	266.2	132.4	-3.8	2.4	0.4	2.4
8	120.0	-350.0	116.9	-348.6	-3.1	1.4	0.7	1.0
9	-400.0	20.0	-403.5	22.4	-3.5	2.4	0.3	1.0
10	340.0	-360.0	341.7	-361.0	1.7	-1.0	5.2	3.4
11	360.0	400.0	356.6	399.7	-3.5	-0.3	5.2	0.7
12	-420.0	440.0	-418.3	442.1	1.7	2.1	5.2	2.4
			average		-2.0	0.7	2.2	2.0

120μm								
group	light (μm)		bead (μm)		offset (μm)		accuracy (μm)	
	X	Y	X	Y	X	Y	ΔX	ΔY
1	0.0	0.0	-3.1	-3.8	-3.1	-3.8		
2	110.0	-60.0	111.4	-59.3	1.4	0.7	4.5	4.5
3	-390.0	80.0	-392.1	82.4	-2.1	2.4	3.4	1.7
4	430.0	-580.0	431.7	-576.6	1.7	3.5	3.8	1.0
5	-330.0	570.0	-334.1	573.1	-4.1	3.1	5.9	0.3
6	-250.0	-440.0	-253.1	-434.8	-3.1	5.2	1.0	2.1
7	-420.0	180.0	-420.7	179.7	-0.7	-0.3	2.4	5.5
8	440.0	-20.0	439.0	-22.1	-1.0	-2.1	0.4	1.7
9	530.0	360.0	527.6	356.6	-2.4	-3.5	1.4	1.4
10	570.0	-30.0	569.3	-28.6	-0.7	1.4	1.7	4.8
11	-240.0	320.0	-237.9	324.5	2.1	4.5	2.8	3.1
12	320.0	-410.0	323.5	-407.9	3.5	2.1	1.4	2.4
			average		-0.7	1.1	2.6	2.6

140μm								
group	light (μm)		bead (μm)		offset (μm)		accuracy (μm)	
	X	Y	X	Y	X	Y	ΔX	ΔY
1	0.0	0.0	-4.1	5.5	-4.1	5.5		
2	-480.0	120.0	-485.5	124.8	-5.5	4.8	1.4	0.7
3	-220.0	300.0	-220.0	302.1	0.0	2.1	5.5	2.8
4	420.0	-330.0	416.6	-325.9	-3.5	4.1	3.5	2.1
5	-270.0	-100.0	-277.6	-96.6	-7.6	3.5	4.1	0.7
6	320.0	-300.0	318.6	-292.4	-1.4	7.6	6.2	4.1
7	-420.0	180.0	-422.1	177.9	-2.1	-2.1	0.7	9.7
8	440.0	-20.0	438.6	-17.2	-1.4	2.8	0.7	4.8
9	530.0	360.0	527.2	360.7	-2.8	0.7	1.4	2.1
10	-240.0	320.0	-247.6	322.1	-7.6	2.1	4.8	1.4
11	320.0	-410.0	315.9	-405.2	-4.1	4.8	3.5	2.8
12	570.0	-30.0	571.4	-27.2	1.4	2.8	5.5	2.1
			average		-3.2	3.2	3.4	3.0

180μm								
group	light (μm)		bead (μm)		offset (μm)		accuracy (μm)	
	X	Y	X	Y	X	Y	ΔX	ΔY
1	0.0	0.0	-11.0	4.1	-11.0	4.1		
2	730.0	-300.0	725.2	-289.7	-4.8	10.4	6.2	6.2
3	-860.0	210.0	-871.7	212.8	-11.7	2.8	6.9	7.6
4	200.0	-620.0	191.7	-606.9	-8.3	13.1	3.5	10.4
5	400.0	90.0	392.4	95.5	-7.6	5.5	0.7	7.6
6	-600.0	220.0	-613.1	230.4	-13.1	10.4	5.5	4.8
7	600.0	-190.0	596.6	-176.9	-3.5	13.1	9.7	2.8
8	-670.0	70.0	-682.4	76.2	-12.4	6.2	9.0	6.9
9	120.0	-100.0	109.7	-95.2	-10.4	4.8	2.1	1.4
10	-510.0	10.0	-527.3	16.9	-17.3	6.9	6.9	2.1
11	610.0	-870.0	599.7	-858.3	-10.4	11.7	6.9	4.8
12	-340.0	-350.0	-351.0	-339.0	-11.0	11.0	0.7	0.7
			average		-10.1	8.3	5.3	5.0

A.2 Speed & Dielectrophoresis Force

Table A.2: Raw Data.

speed (µm/s)	60µm											
	5 frames					average	5 frames					standard deviation
	pixel						µm					
2800	41	42	38	41	39	40.2	29.52	30.24	27.36	29.52	28.08	1.183080724
2500	28	29	25	27	26	27	20.16	20.88	18	19.44	18.72	1.138419958
2300	19	24	23	22	22	22	13.68	17.28	16.56	15.84	15.84	1.346996659
2100	18	17	16	18	18	17.4	12.96	12.24	11.52	12.96	12.96	0.643987578
1800	17	18	15	18	17	17	12.24	12.96	10.8	12.96	12.24	0.881816307
1500	13	13	13	12	12	12.6	9.36	9.36	9.36	8.64	8.64	0.394360241
1200	9	11	10	9	10	9.8	6.48	7.92	7.2	6.48	7.2	0.602395219
900	8	8	8	9	8	8.2	5.76	5.76	5.76	6.48	5.76	0.321993789
600	4	5	4	5	4	4.4	2.88	3.6	2.88	3.6	2.88	0.394360241
400	4	5	4	4	4	4.2	2.88	3.6	2.88	2.88	2.88	0.321993789
300	1	1	1	2	1	1.2	0.72	0.72	0.72	1.44	0.72	0.321993789
200	1	1	1	1	0	0.8	0.72	0.72	0.72	0.72	0	0.321993789
100	0	0	1	0	0	0.2	0	0	0.72	0	0	0.321993789

speed (µm/s)	100µm											
	5 frames					average	5 frames					standard deviation
	pixel						µm					
2800	67	64	73	78	74	71.2	48.24	46.08	52.56	56.16	53.28	4.053798219
2500	61	58	55	61	62	59.4	43.92	41.76	39.6	43.92	44.64	2.074299882
2300	56	56	57	58	55	56.4	40.32	40.32	41.04	41.76	39.6	0.820926306
2100	54	54	54	55	55	54.4	38.88	38.88	38.88	39.6	39.6	0.394360241
1800	48	48	48	47	48	47.8	34.56	34.56	34.56	33.84	34.56	0.321993789
1500	43	43	43	42	43	42.8	30.96	30.96	30.96	30.24	30.96	0.321993789
1200	39	38	38	38	39	38.4	28.08	27.36	27.36	27.36	28.08	0.394360241
900	32	32	32	32	30	31.6	23.04	23.04	23.04	23.04	21.6	0.643987578
600	27	26	27	26	27	26.6	19.44	18.72	19.44	18.72	19.44	0.394360241
400	20	20	20	19	20	19.8	14.4	14.4	14.4	13.68	14.4	0.321993789
300	16	17	16	17	16	16.4	11.52	12.24	11.52	12.24	11.52	0.394360241
200	9	9	9	10	9	9.2	6.48	6.48	6.48	7.2	6.48	0.321993789
100	8	7	8	7	7	7.4	5.76	5.04	5.76	5.04	5.04	0.394360241

speed (µm/s)	140µm											
	5 frames					average	5 frames					standard deviation
	pixel						µm					
2500	103	110	113	110	110	109.2	74.16	79.2	81.36	79.2	79.2	2.664972795
2300	99	99	96	95	98	97.4	71.28	71.28	69.12	68.4	70.56	1.307944953
2100	89	91	88	87	89	88.8	64.08	65.52	63.36	62.64	64.08	1.067932582
1800	83	81	82	81	81	81.6	59.76	58.32	59.04	58.32	58.32	0.643987578
1500	75	75	74	74	73	74.2	54	54	53.28	53.28	52.56	0.602395219
1200	66	66	66	67	67	66.4	47.52	47.52	47.52	48.24	48.24	0.394360241
900	60	58	59	59	60	59.2	43.2	41.76	42.48	42.48	43.2	0.602395219
600	48	48	49	48	46	47.8	34.56	34.56	35.28	34.56	33.12	0.788720483
400	36	36	38	37	35	36.4	25.92	25.92	27.36	26.64	25.2	0.820926306
300	28	27	27	28	28	27.6	20.16	19.44	19.44	20.16	20.16	0.394360241
200	18	18	18	18	17	17.8	12.96	12.96	12.96	12.96	12.24	0.321993789
100	6	6	7	7	6	6.4	4.32	4.32	5.04	5.04	4.32	0.394360241

speed (µm/s)	180µm											
	5 frames					average	5 frames					standard deviation
	pixel						µm					
2500	133	136	132	141	133	135	95.76	97.92	95.04	101.52	95.76	2.645448922
2300	125	128	126	125	129	126.6	90	92.16	90.72	90	92.88	1.307944953
2100	123	124	125	123	125	124	88.56	89.28	90	88.56	90	0.72
1800	108	108	109	108	108	108.2	77.76	77.76	78.48	77.76	77.76	0.321993789
1500	102	105	103	103	103	103.2	73.44	75.6	74.16	74.16	74.16	0.788720483
1200	94	94	94	95	94	94.2	67.68	67.68	67.68	68.4	67.68	0.321993789
900	85	85	85	86	86	85.4	61.2	61.2	61.2	61.92	61.92	0.394360241
600	67	67	67	69	68	67.6	48.24	48.24	48.24	49.68	48.96	0.643987578
400	48	50	50	46	49	48.6	34.56	36	36	33.12	35.28	1.204790438
300	36	36	35	32	40	35.8	25.92	25.92	25.2	23.04	28.8	2.061766233
200	23	22	22	23	26	23.2	16.56	15.84	15.84	16.56	18.72	1.183080724
100	16	16	16	15	15	15.6	11.52	11.52	11.52	10.8	10.8	0.394360241

Table A.3: Speed & Dielectrophoresis Force.

speed (μm/s)	force (nN)	60μm					100μm				
		pixel			μm		pixel			μm	
		offset	average	difference	distance	error bar	offset	average	difference	distance	error bar
2800	-3.27447	-1	40.2	41.2	29.664	1.183081	7	71.2	64.2	46.224	4.053798
2500	-2.92363	-1	27	28	20.16	1.13842	4	59.4	55.4	39.888	2.0743
2300	-2.68974	-1	22	23	16.56	1.346997	6	56.4	50.4	36.288	0.820926
2100	-2.45585	-1	17.4	18.4	13.248	0.643988	6	54.4	48.4	34.848	0.39436
1800	-2.10502	-1	17	18	12.96	0.881816	6	47.8	41.8	30.096	0.321994
1500	-1.75418	-1	12.6	13.6	9.792	0.39436	5	42.8	37.8	27.216	0.321994
1200	-1.40334	-1	9.8	10.8	7.776	0.602395	6	38.4	32.4	23.328	0.39436
900	-1.05251	-1	8.2	9.2	6.624	0.321994	6	31.6	25.6	18.432	0.643988
600	-0.70167	-1	4.4	5.4	3.888	0.39436	6	26.6	20.6	14.832	0.39436
400	-0.46778	-1	4.2	5.2	3.744	0.321994	6	19.8	13.8	9.936	0.321994
300	-0.35084	-1	1.2	2.2	1.584	0.321994	5	16.4	11.4	8.208	0.39436
200	-0.23389	-1	0.8	1.8	1.296	0.321994	7	9.2	2.2	1.584	0.321994
100	-0.11695	-1	0.2	1.2	0.864	0.321994	7	7.4	0.4	0.288	0.39436
-100	0.116945	-1	0.2	-1.2	-0.864	0.321994	7	7.4	-0.4	-0.288	0.39436
-200	0.233891	-1	0.8	-1.8	-1.296	0.321994	7	9.2	-2.2	-1.584	0.321994
-300	0.350836	-1	1.2	-2.2	-1.584	0.321994	5	16.4	-11.4	-8.208	0.39436
-400	0.467781	-1	4.2	-5.2	-3.744	0.321994	6	19.8	-13.8	-9.936	0.321994
-600	0.701672	-1	4.4	-5.4	-3.888	0.39436	6	26.6	-20.6	-14.832	0.39436
-900	1.052508	-1	8.2	-9.2	-6.624	0.321994	6	31.6	-25.6	-18.432	0.643988
-1200	1.403344	-1	9.8	-10.8	-7.776	0.602395	6	38.4	-32.4	-23.328	0.39436
-1500	1.754181	-1	12.6	-13.6	-9.792	0.39436	5	42.8	-37.8	-27.216	0.321994
-1800	2.105017	-1	17	-18	-12.96	0.881816	6	47.8	-41.8	-30.096	0.321994
-2100	2.455853	-1	17.4	-18.4	-13.248	0.643988	6	54.4	-48.4	-34.848	0.39436
-2300	2.689743	-1	22	-23	-16.56	1.346997	6	56.4	-50.4	-36.288	0.820926
-2500	2.923634	-1	27	-28	-20.16	1.13842	4	59.4	-55.4	-39.888	2.0743
-2800	3.27447	-1	40.2	-41.2	-29.664	1.183081	7	71.2	-64.2	-46.224	4.053798

speed (μm/s)	force (nN)	140μm					180μm				
		pixel			μm		pixel			μm	
		offset	average	difference	distance	error bar	offset	average	difference	distance	error bar
2500	-2.92363	-2	109.2	111.2	80.064	2.664973	-2	135	137	98.64	2.64545
2300	-2.68974	-5	97.4	102.4	73.728	1.307945	-6	126.6	132.6	95.472	1.30794
2100	-2.45585	-3	88.8	91.8	66.096	1.067933	-2	124	126	90.72	0.72
1800	-2.10502	-3	81.6	84.6	60.912	0.643988	1	108.2	107.2	77.184	0.32199
1500	-1.75418	-2	74.2	76.2	54.864	0.602395	-2	103.2	105.2	75.744	0.78872
1200	-1.40334	-2	66.4	68.4	49.248	0.39436	-3	94.2	97.2	69.984	0.32199
900	-1.05251	-2	59.2	61.2	44.064	0.602395	-4	85.4	89.4	64.368	0.39436
600	-0.70167	-1	47.8	48.8	35.136	0.78872	-3	67.6	70.6	50.832	0.64399
400	-0.46778	1	36.4	35.4	25.488	0.820926	8	48.6	40.6	29.232	1.20479
300	-0.35084	-1	27.6	28.6	20.592	0.39436	2	35.8	33.8	24.336	2.06177
200	-0.23389	1	17.8	16.8	12.096	0.321994	7	23.2	16.2	11.664	1.18308
100	-0.11695	1	6.4	5.4	3.888	0.39436	4	15.6	11.6	8.352	0.39436
-100	0.116945	1	6.4	-5.4	-3.888	0.39436	4	15.6	-11.6	-8.352	0.39436
-200	0.233891	1	17.8	-16.8	-12.096	0.321994	7	23.2	-16.2	-11.664	1.18308
-300	0.350836	-1	27.6	-28.6	-20.592	0.39436	2	35.8	-33.8	-24.336	2.06177
-400	0.467781	1	36.4	-35.4	-25.488	0.820926	8	48.6	-40.6	-29.232	1.20479
-600	0.701672	-1	47.8	-48.8	-35.136	0.78872	-3	67.6	-70.6	-50.832	0.64399
-900	1.052508	-2	59.2	-61.2	-44.064	0.602395	-4	85.4	-89.4	-64.368	0.39436
-1200	1.403344	-2	66.4	-68.4	-49.248	0.39436	-3	94.2	-97.2	-69.984	0.32199
-1500	1.754181	-2	74.2	-76.2	-54.864	0.602395	-2	103.2	-105.2	-75.744	0.78872
-1800	2.105017	-3	81.6	-84.6	-60.912	0.643988	1	108.2	-107.2	-77.184	0.32199
-2100	2.455853	-3	88.8	-91.8	-66.096	1.067933	-2	124	-126	-90.72	0.72
-2300	2.689743	-5	97.4	-102.4	-73.728	1.307945	-6	126.6	-132.6	-95.472	1.30794
-2500	2.923634	-2	109.2	-111.2	-80.064	2.664973	-2	135	-137	-98.64	2.64545

Appendix B

Full Data of the 50 μm Silver-coated PMMA Microspheres

B.1 Displacements & Accuracy

Table B.1: Displacements & Accuracy.

60μm								
group	light (μm)		bead (μm)		offset (μm)		accuracy (μm)	
	X	Y	X	Y	X	Y	ΔX	ΔY
1	0.0	0.0	-1.4	-1.4	-1.4	-1.4		
2	290.0	250.0	289.3	249.3	-0.7	-0.7	0.7	0.7
3	100.0	-240.0	98.6	-241.0	-1.4	-1.0	0.7	0.3
4	-160.0	270.0	-161.0	269.0	-1.0	-1.0	0.3	0.0
5	210.0	-90.0	208.3	-91.0	-1.7	-1.0	0.7	0.0
6	-20.0	120.0	-21.0	119.0	-1.0	-1.0	0.7	0.0
7	-180.0	90.0	-181.4	89.0	-1.4	-1.0	0.3	0.0
8	130.0	-280.0	129.0	-280.3	-1.0	-0.3	0.3	0.7
9	70.0	220.0	69.0	219.3	-1.0	-0.7	0.0	0.4
10	1330.0	-250.0	1329.3	-250.7	-0.7	-0.7	0.3	0.0
11	-180.0	170.0	-181.4	169.0	-1.4	-1.0	0.7	0.3
12	50.0	140.0	49.3	139.3	-0.7	-0.7	0.7	0.3
			average		-1.1	-0.9	0.5	0.3

100μm								
group	light (μm)		bead (μm)		offset (μm)		accuracy (μm)	
	X	Y	X	Y	X	Y	ΔX	ΔY
1	0.0	0.0	-3.5	2.1	-3.5	2.1		
2	70.0	-500.0	67.9	-497.9	-2.1	2.1	1.4	0.0
3	-470.0	160.0	-473.5	161.4	-3.5	1.4	1.4	0.7
4	-50.0	-70.0	-53.8	-68.6	-3.8	1.4	0.4	0.0
5	-50.0	280.0	-52.1	280.3	-2.1	0.3	1.7	1.0
6	180.0	-20.0	178.6	-19.3	-1.4	0.7	0.7	0.4
7	-90.0	60.0	-93.1	62.1	-3.1	2.1	1.7	1.4
8	380.0	-330.0	377.6	-328.3	-2.4	1.7	0.7	0.3
9	-130.0	-440.0	-132.4	-438.6	-2.4	1.4	0.0	0.3
10	200.0	140.0	196.9	141.7	-3.1	1.7	0.7	0.3
11	-180.0	240.0	-182.1	242.1	-2.1	2.1	1.0	0.3
12	400.0	390.0	397.9	390.3	-2.1	0.3	0.0	1.7
			average		-2.6	1.4	0.9	0.6

150μm								
group	light (μm)		bead (μm)		offset (μm)		accuracy (μm)	
	X	Y	X	Y	X	Y	ΔX	ΔY
1	0.0	0.0	0.4	7.2	0.4	7.2		
2	100.0	310.0	98.3	311.9	-1.7	1.9	2.1	5.3
3	320.0	580.0	315.9	588.6	-4.1	8.6	2.4	6.7
4	110.0	-120.0	107.2	-111.4	-2.8	8.6	1.4	0.0
5	-100.0	-590.0	-107.3	-581.4	-7.3	8.6	4.5	0.0
6	560.0	640.0	555.9	648.3	-4.1	8.3	3.1	0.3
7	-740.0	310.0	-741.7	318.3	-1.7	8.3	2.4	0.0
8	690.0	-10.0	689.3	-1.4	-0.7	8.6	1.0	0.4
9	230.0	740.0	226.9	747.6	-3.1	7.6	2.4	1.0
10	-330.0	540.0	-331.7	548.3	-1.7	8.3	1.4	0.7
11	320.0	-60.0	318.6	-51.4	-1.4	8.6	0.4	0.4
12	-340.0	0.0	-340.0	8.6	0.0	8.6	1.4	0.0
			average		-2.4	7.8	2.0	1.3

200μm								
group	light (μm)		bead (μm)		offset (μm)		accuracy (μm)	
	X	Y	X	Y	X	Y	ΔX	ΔY
1	0.0	0.0	-3.5	5.9	-3.5	5.9		
2	-370.0	810.0	-367.2	816.6	2.8	6.6	6.2	0.7
3	190.0	-950.0	196.2	-951.4	6.2	-1.4	3.5	7.9
4	-880.0	-330.0	-876.9	-323.8	3.1	6.2	3.1	7.6
5	250.0	-180.0	250.0	-171.7	0.0	8.3	3.1	2.1
6	40.0	-600.0	41.4	-593.8	1.4	6.2	1.4	2.1
7	240.0	740.0	237.2	743.8	-2.8	3.8	4.1	2.4
8	-710.0	50.0	-703.4	52.1	6.6	2.1	9.3	1.7
9	10.0	-30.0	9.0	-35.2	-1.0	-5.2	7.6	7.2
10	770.0	-200.0	768.3	-200.0	-1.7	0.0	0.7	5.2
11	-30.0	840.0	-30.0	839.0	0.0	-1.0	1.7	1.0
12	730.0	-710.0	732.8	-709.0	2.8	1.0	2.8	2.1
			average		1.2	2.7	4.0	3.6

Appendix C

Full Data of Current-Voltage Characteristic

Table C.1: Full Data of Current-Voltage Characteristic.

Voltage (V)	Current (A)
0	9.54E-08
0.05	0.00433
0.1	0.00867
0.15	0.01299
0.2	0.01732
0.25	0.02164
0.3	0.02596
0.35	0.03028
0.4	0.03457
0.45	0.03886
0.5	0.04313
0.55	0.0474
0.6	0.05164
0.65	0.05588
0.7	0.06009
0.75	0.06428
0.8	0.06845
0.85	0.0726
0.9	0.07672
0.95	0.08081
1	0.08488

Appendix D

Full Data of Moving Distance

Table D.1: Full Data of Moving Distance.

bead No.	group 1 - moving distance					
	x (pixcel)	y (pixcel)	d (pixcel)	x (μm)	y (μm)	d (μm)
1	41	-42	58.69412	20.5	-21	29.34706
2	49	-16	51.5461	24.5	-8	25.77305
3	74	23	77.49194	37	11.5	38.74597
			average	27.33333	-5.83333	31.28869

bead No.	group 2 - moving distance					
	x (pixcel)	y (pixcel)	d (pixcel)	x (μm)	y (μm)	d (μm)
4	-27	6	27.65863	-14.7945	3.287671	15.15542
5	-24	8	25.29822	-13.1507	4.383562	13.86204
6	-44	43	61.52235	-24.1096	23.56164	33.71088
7	-13	88	88.95504	-7.12329	48.21918	48.74249
8	-16	30	34	-8.76712	16.43836	18.63014
9	-34	-5	34.36568	-18.6301	-2.73973	18.83051
10	-30	2	30.06659	-16.4384	1.09589	16.47485
			average	-14.7162	13.4638	23.62947

overall average	25.92724